SEDIMENTOLOGY the journal of the International Association of Sedimentologists

Sedimentology (2020) **67**, 849–881 doi: 10.1111/sed.12664

Testing the preservation potential of early diagenetic dolomites as geochemical archives

MATHIAS MUELLER*, ONYEDIKA A. IGBOKWE*†, BENJAMIN WALTER‡§, CHELSEA L. PEDERSON*, SYLVIA RIECHELMANN*, DETLEV K. RICHTER*, RICHARD ALBERT¶, AXEL GERDES¶, DIETER BUHL*, ROLF D. NEUSER*, GIOVANNI BERTOTTI** and ADRIAN IMMENHAUSER*

**Institute of Geology, Mineralogy and Geophysics, Ruhr-University Bochum, Universitätsstraße 150, Bochum 44801, Germany (E-mail: mathias.mueller-l1y@rub.de)*

†Department of Geology, Alex Ekwueme Federal University Ndufu-Alike, P.M.B. 1010, Ikwo, Abakaliki, Ebonyi State, Nigeria

‡Department of Geoscience, University of Tübingen, Wilhelmstraße 56, Tübingen 72074, Germany

§AGW Institute for Applied Geoscience, Karlsruhe Institute for Technology, Campus South, Adenauering 20b, Karlsruhe 76131, Germany

¶Institute of Geosciences, Goethe-University Frankfurt, Altenhöferallee 1, Frankfurt am Main 60438, Germany

***Faculty of Civil Engineering and Geosciences, TU Delft, Stevinweg 1, Delft 2628 CN, The Netherlands*

Associate Editor – Hairuo Qing

ABSTRACT

Early marine diagenetic dolomite is a rather thermodynamically-stable carbonate phase and has potential to act as an archive of marine porewater properties. However, the variety of early to late diagenetic dolomite phases that can coexist within a single sample can result in extensive complexity. Here, the archive potential of early marine dolomites exposed to extreme post-depositional processes is tested using various types of analyses, including: petrography, fluid inclusion data, stable $\delta^{13}C$ and $\delta^{18}O$ isotopes, $^{87}Sr/^{86}Sr$ ratios, and U-Pb age dating of various dolomite phases. In this example, a Triassic carbonate platform was dissected and overprinted (diagenetic temperatures of 50 to 430°C) in a strike-slip zone in Southern Spain. Eight episodes of dolomitization, a dolostone cataclasite and late stage meteoric/vadose cementation were recognized. The following processes were found to be diagenetically relevant: (i) protolith deposition and fabric-preservation, and marine dolomitization of precursor aragonite and calcite during the Middle–Late Triassic; (ii) intermediate burial and formation of zebra saddle dolomite and precipitation of various dolomite cements in a Proto-Atlantic opening stress regime (*T ca* 250°C) during the Early–Middle Jurassic; (iii) dolomite cement precipitation during early Alpine tectonism, rapid burial to *ca* 15 km, and high-grade anchizone overprint during Alpine tectonic evolution in the Early Eocene to Early Miocene; (iv) brecciation of dolostones to cataclasite during the onset of the Carboneras Fault Zone activity during the Middle Miocene; and (v) late-stage regression and subsequent meteoric overprint. Data shown here document that, under favourable conditions, early diagenetic marine dolomites and their archive data may resist petrographic and geochemical resetting over time intervals of 10^8 or more years. Evidence for this preservation includes preserved Late Triassic seawater $\delta^{13}C_{DIC}$ values and primary fluid inclusion data. Data also indicate that oversimplified statements

based on bulk data from other petrographically-complex dolomite archives must be considered with caution.

Keywords Diagenesis, dolomite, dolomitization, fluid inclusions, geochemistry, petrography, tectonic overprint, U-Pb dating.

INTRODUCTION

Stoichiometric dolomites (dolostones) are the most thermodynamically-stable carbonate phase, surpassing even low-Mg calcites, which have been referred to as the most reliable archives of their depositional environment (Nordeng & Sibley, 1994). This also holds true with respect to earliest diagenetic marine dolomites. Previous studies have exploited these carbonates as archives of their palaeo-porewater properties (Geske *et al.*, 2012), often with reference to replacement dolostones or primary dolomite precipitates in modern sabkha and peritidal–supratidal settings (Land, 1980; Patterson & Kinsman, 1982) or in various ancient carbonate deposits (Mazumdar & Strauss, 2006; Johnston *et al.*, 2010; Kasemann *et al.*, 2014). These authors argued that fabric-preserving, early diagenetic marine dolomites may largely escape subsequent alteration. Considering the mineral chemistry and temperature-dependent fractionation patterns between fluids and minerals, early diagenetic dolomites offer insight into time-resolved patterns in marine dynamics (Halverson *et al.*, 2005; Geske *et al.*, 2012). Other research questions included the redox state of past oceans (Kamber & Webb, 2001; Hood *et al.*, 2018), element fluxes between oceans and continents (Tipper *et al.*, 2006), and the geochemical cycles of C, Ca and Mg through time (Arvidson *et al.*, 2006; Farkaš *et al.*, 2007; Arvidson *et al.*, 2011).

Despite their potential, ancient dolostone archives as proxies of their palaeoenvironment are also under debate (Halverson *et al.*, 2005; Mazumdar & Strauss, 2006; Derry, 2010a,b; Frimmel, 2010; Johnston *et al.*, 2010; Nagarajan *et al.*, 2013; Kasemann *et al.*, 2014). Problems include the influence of microbial metabolisms (Bontognali *et al.*, 2010; Petrash *et al.*, 2017), as well as a common non-stoichiometric (or even amorphous; Mavromatis *et al.*, 2017) nature at precipitation, resulting in complex fluid–mineral interaction. Moreover, marine porewaters may display variable degrees of isolation from the overlying seawater body. Acknowledging these issues (Sandberg, 1983; Hardie, 1996; Qing *et al.*, 2001; Derry, 2010a; Rott & Qing, 2013; Zohdi *et al.*, 2014; Geske *et al.*, 2015a,b), the resistance of early marine dolomites to a wide range of post-depositional processes is systematically tested using a Triassic example from southern Spain, where early marine diagenetic dolomites (Martín, 1978; Martín & Braga, 1987) were exposed to extreme conditions in a regionally important strike-slip zone (Kampschuur & Rondeel, 1975; Weijermars, 1991; Keller *et al.*, 1995; Faulkner *et al.*, 2003; Platt *et al.*, 2005; Faulkner *et al.*, 2008; Rutter *et al.*, 2012; Sola *et al.*, 2018). This region represents a natural laboratory to test the preservation potential of these archives. A limitation of this case study (which is a common problem) includes the difficulty in reconstructing Mesozoic 'aragonite sea' seawater properties (e.g. Sandberg, 1983; Hardie, 1996). Hence, assumptions are made regarding the fractionation between marine porewaters and early non-stoichiometric dolomites (Land, 1980; McKenzie, 1981; Patterson & Kinsman, 1982; Wacey *et al.*, 2007). Given that the authors do not aim to reconstruct Triassic marine porewater properties, but rather to assess the response of early marine diagenetic dolomites to burial and meteoric diagenetic fluids over large time frames (>10^8 years), the limitations are considered to be reasonable.

The aims of this paper are three-fold; (i) to identify the complex diagenetic pathways of allochthonous Triassic dolostones in the Neogene Carboneras Fault Zone in Southern Spain by mineralogy, petrology and (isotope) geochemistry; (ii) to place these findings into context of hydrothermal fluid properties reconstructed from fluid inclusion data and geochemical fingerprints; and (iii) to test the resistance of a suite of early diagenetic dolostones to mechanical and hydrothermal alteration culminating in cataclastic fault gouge formation. This study provides a basis for the reconstruction of post-sedimentary dolostone diagenesis that may be linked to discrete tectonic events, palaeoenvironmental changes, subsurface fluid chemistry and circulation patterns. These data also suggest limitations concerning the value of bulk

dolostone chemostratigraphy in interpreting diagenetic histories.

GEOLOGICAL BACKGROUND

This study focuses on the northern portion of the Carboneras Fault Zone in south-east Spain (Fig. 1). The fault zone is a large-scale, north-east/south-west oriented lineament in the Betic Cordillera, and has been active since the Late Serravallian (Neogene). The major phase of fault movement occurred between 12 Ma and 6 Ma (Rutter *et al.*, 2012, 2014; Moreno *et al.*, 2015). The Carboneras Fault Zone separates the volcanic Cabo de Gata province to the south, from the uplifted Alpine metamorphic basement blocks and Neogene basins to the north (Kampschuur & Rondeel, 1975; Rutter *et al.*, 2012, 2014). The Palaeozoic to Mesozoic basement rocks consist of three tectonic units. The lowest unit is the Nevado–Filabride Complex, characterized by upper greenschist facies, mica schists and quartzites (Kampschuur & Rondeel, 1975; Torres-Roldán, 1979; Platt & Vissers, 1989; Lonergan & Platt, 1995). This is tectonically overlain by phyllites, followed by Anisian–Rhaetian dolostones (Fig. 2) of the Triassic Alpujarride nappe (Kampschuur & Rondeel, 1975; Delgado *et al.*, 1981; Martín & Braga, 1987; Faulkner *et al.*, 2003; Platt *et al.*, 2005). The uppermost tectonic wedge contains dolostones capping non-metamorphic clastics and various carbonate units, including Ladinian–Liassic (Triassic–Jurassic) dolostones belonging to the Upper Triassic to Palaeogene Maláguide unit (Lonergan, 1993). The two dolostone units, or their respective precursor facies, were deposited on a Tethyan carbonate platform (Roep, 1972; Martín & Braga, 1987; Sanz de Galdeano *et al.*, 2001). In the Betic Cordillera, tectono-metamorphic activity during the Alpine Orogeny peaked in the Early Miocene (25 to 18 Ma), resulting in three tectonic assemblages, with an upward decrease in metamorphosis (Platt & Vissers, 1989; Alonso-Chaves *et al.*, 2004; Vissers, 2012). The Malaguide complex largely avoided metamorphism during the latest stages of the Alpine Orogeny, while the Alpujarride rocks became exposed to low-grade greenschist metamorphism (Lonergan, 1993; Vissers, 2012). Volcanic and volcanoclastic horizons of the Cabo de Gata province developed in three pulses between 18 Ma and 6 Ma, accompanied by intrusions into the fault zone (Rutter *et al.*, 2012).

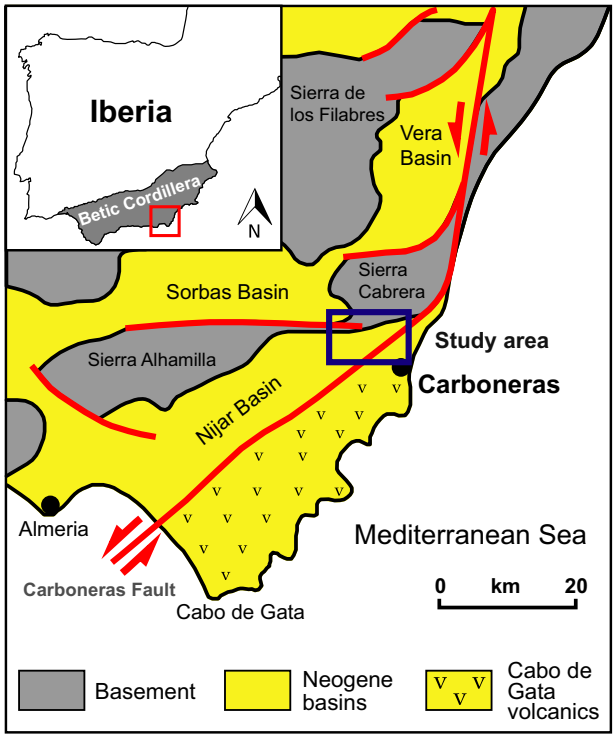

Fig. 1. Map of south-east Spain showing the location of uplifted basement blocks and Neogene basins in the vicinity of the onshore area of the Carboneras Fault. The whole area covers the internal Betic Cordillera. The study area is indicated by the blue box. Modified from Rutter *et al.* (2012).

Formation of the Carboneras Nijar Basin (Figs 1 and 2A) was initiated by regional subsidence and subsequent marine ingression. The lower Serravallian/early Tortonian marls of the Saltador Formation represent the oldest marine sediments (Van de Poel, 1992; Fortuin & Krijgsman, 2003). The Saltador is overlain unconformably to the north by the fossiliferous calcarenite and marls of the Azagador Formation (Völk & Rondeel, 1964; Fortuin & Krijgsman, 2003), which rest directly on basement rocks (Figs 2A, 3 and 4). The Azagador is in turn overlain unconformably by three Messinian (Neogene) formations: The Abad (marls), the Yesares (Messinian Salinity Crisis gypsum) and the Feos (marls; Fortuin & Krijgsman, 2003). These Messinian deposits are overlain by Pliocene (Neogene) horizons, which are inclined towards the south of the Sierra Cabrera. The younger units are progressively less inclined, indicating progressive uplift (Martín *et al.*, 2003). Following the predominance of marine conditions during the Serravallian to Pliocene, the Pleistocene glaciation intervals resulted in drying of the basin and

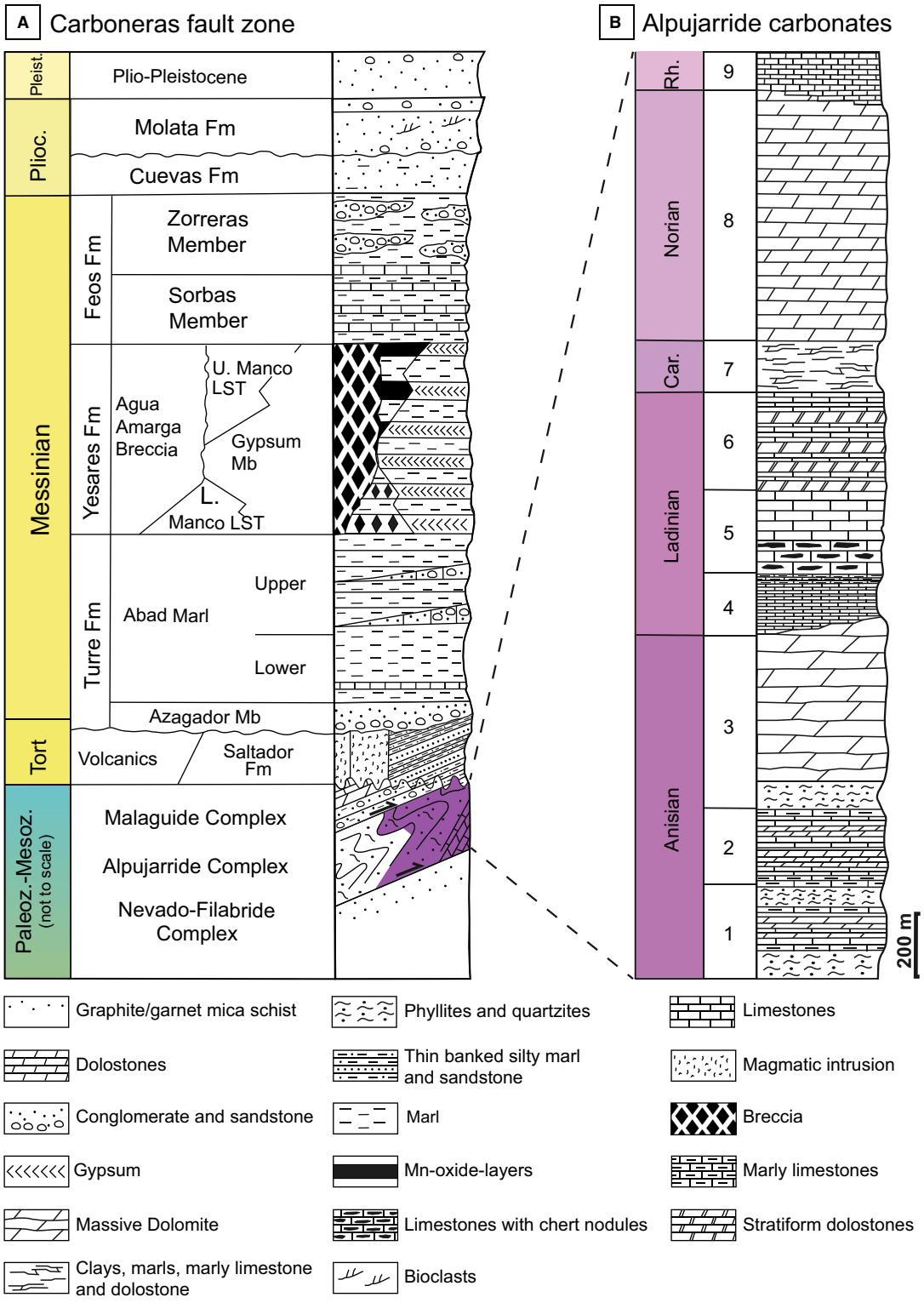

Fig. 2. Generalized stratigraphic columns for: (A) the Carboneras Fault Zone (not to scale, modified from Keller *et al.*, 1995); and (B) the Triassic carbonates of the Alpujarride complex in the Betic Cordillera (from Martín & Braga, 1987). Note that the Alpujarride carbonates occur exclusively as faulted blocks in the study area. Therefore, no assignment to specific formations was carried out, and all stratigraphical ranges in the figures are given accordingly for the Anisian–Rhaetian (Middle/Late Triassic) time interval. Refer to Martín & Braga (1987) for details and depositional settings of the individual facies types 1 to 9. LST, limestone.

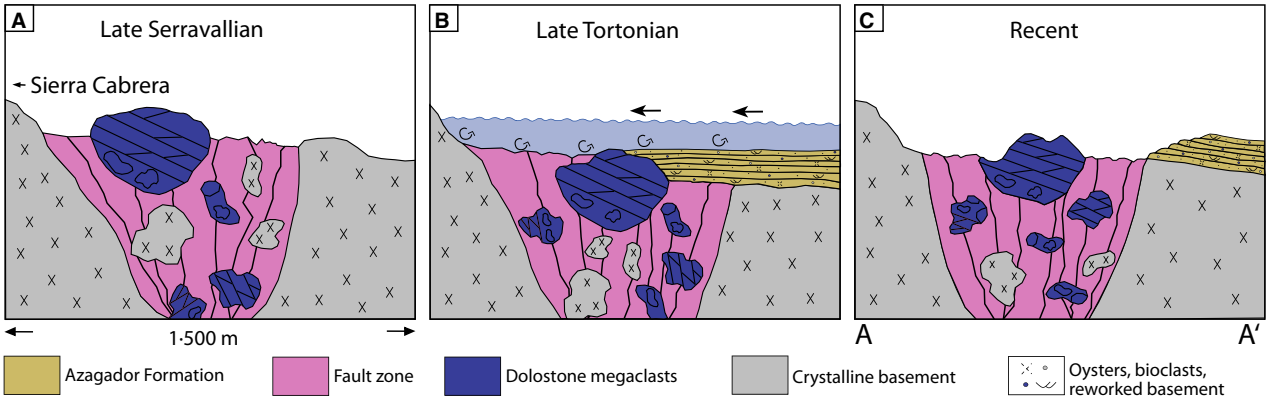

Fig. 3. Schematic showing the Neogene–Recent geological evolution in the studied dolostones and surrounding strata of this study (depth not to scale). (A) Late Serravallian. The main activity phase of the Carboneras Fault Zone used zones of structural weakness between Alpujarride crystalline and carbonate rocks and likely generated dolostone blocks that float in the upper part of the fault zone. (B) Local subsidence of the Nijar Basin in the South results in partial erosion of basement rocks and deposition of shallow marine calcarenites of the Azagador Formation. (C) Uplift of the Sierra Cabrera in the north and eustatic marine regression resulted in the recent condition.

subaerial exhumation of the fault zone. For additional information about the regional geology see Rutter *et al.* (2012). A summary of the Neogene to Recent settings in the study area is shown in Fig. 3.

MATERIALS AND METHODS

Sampling strategy

The Alpujarride dolostones were chosen for this study due to their abundance and diverse range of hydrothermal and tectonic overprint in a well-exposed 'natural laboratory', in addition to their well-established regional and tectonic framework (Rutter *et al.*, 2012, 2014, and references therein). Fieldwork was mainly performed in the northern strand of the Carboneras Fault Zone (Fig. 4) in areas of structural and hydrothermal overprint. To assess the complete paragenetic sequence, all variations of petrographic features observable in the field, such as veins and cements, were sampled. To analyze the diagenetic evolution from early alteration features to brecciated and cataclastic dolostone, the paragenetic phases were characterized by thin section and geochemical analyses. In order to provide context for dolostones and dolomite cements, calcitic autochthonous Messinian sedimentary rocks from the Carboneras Nijar Basin (including bivalve shells), subrecent soil carbonates (caliche) and a calcitic speleothem were analyzed.

Origin and field aspects of dolostones investigated

Dolostone blocks are highly variable in size (<1 m to 2 km) and are widespread across the Carboneras Fault Zone. Basement blocks and Neogene units of the Carboneras–Nijar Basin are embedded in a fine-grained clay mineral rich fault gouge matrix (Fig. 5A). Due to lack of age assigning fossils, Alpujarride (Fig. 2B) and Malaguide dolostones were differentiated based on macroscopic criteria (dark-grey versus light weathering colour), the presence of dolomitized ooids and the field association of the Malaguide dolostones with red siltstones. Siltstones do not crop out in the northern part of the Carboneras Fault Zone and Malaguide dolostones are less common in the study area compared to the region south of the southern strand of the Carboneras Fault Zone (Rutter *et al.*, 2012). The focus in this study is on Alpujarride dolostones (72 samples), but a limited number (14 samples) of Malaguide dolostones were also studied. The latter samples were included to test whether data from stratigraphically younger Malaguide dolostones, accidentally sampled as Alpujarride dolostones, deviate significantly from the stratigraphically older Alpujarride dolostones.

Petrographic, mineralogical and fluid inclusion analysis of dolostones

A total of 49 thin sections were analyzed using polarized and cathodoluminescence microscopy.

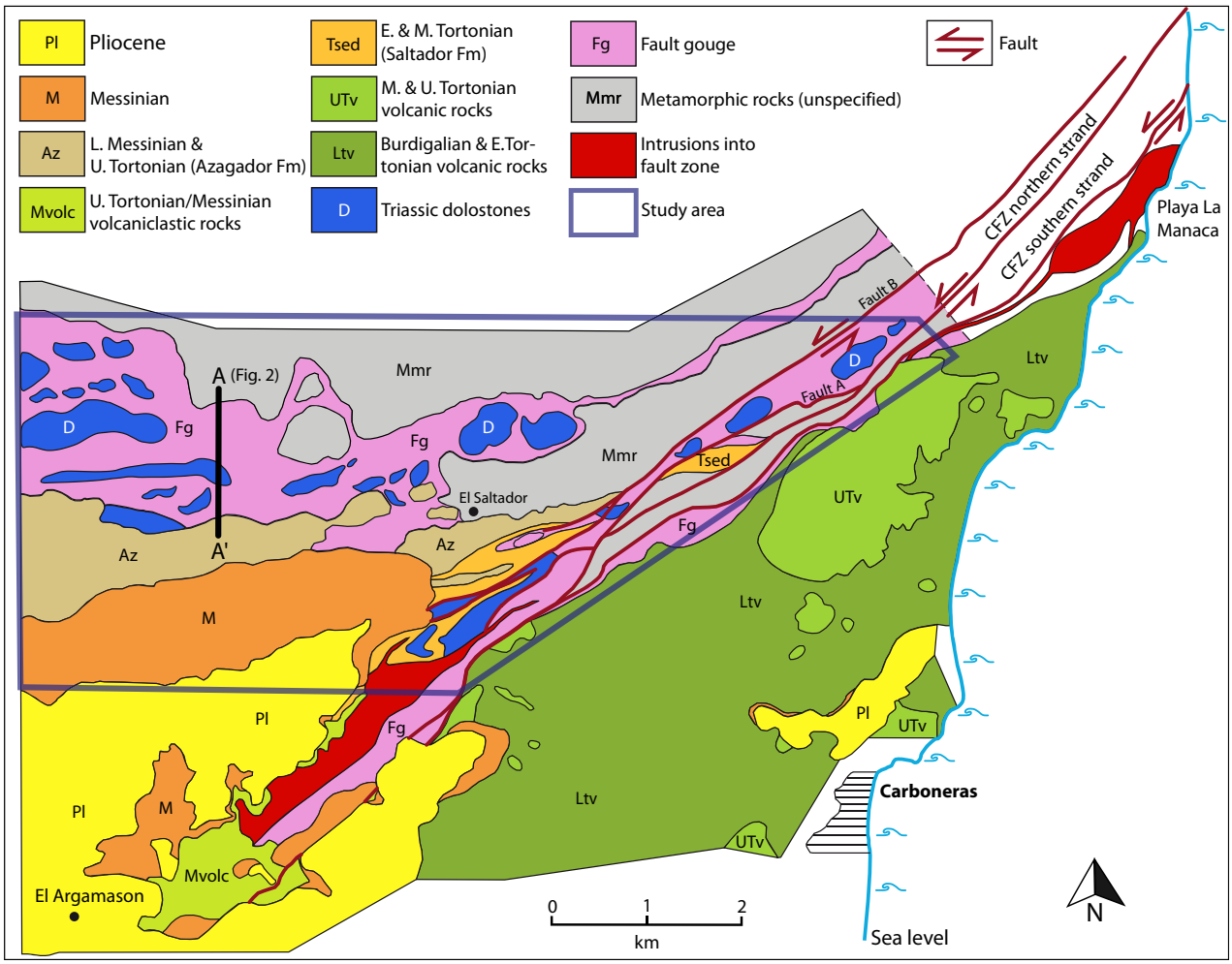

Fig. 4. Geological map of the Carboneras Fault Zone (CFZ). The map was generated using the data of Rutter *et al.*, 2012, and complemented (in the northern part) with data generated in this study. It shows the Neogene–Quarternary deposits of the Carboneras Nijar Basin and underlying basement rocks being faulted by the Carboneras Fault Zone. The study area is outlined in blue, and the location of the schematic section in Fig. 3 is indicated as A to A'. Formation names are based on those used by Van de Poel (1992), Fortuin & Krijgsman (2003) and Rutter *et al.* (2012), with some modification.

The polarized images were taken on a Leica DM4500P microscope (Leica Microsystems GmbH, Wetzlar, Germany). Cathodoluminescence analyses were performed using a hot cathode (HC1-LM) facility developed at the Ruhr-University Bochum (Neuser *et al.*, 1996) equipped with a DC73 video camera system (Olympus, Hamburg, Germany). The thin sections were sputter coated with a 15 nm thick gold layer to avoid charging. The electron beam had an acceleration voltage of the 14 kV, current density from 5 to 10 μA mm^{-2}, and beam current between 0·1 mA and 0·2 mA.

Microthermometric analyses were performed using a Linkam THMS600 stage (Linkam Scientific, Tadworth, UK) at the University of Tübingen, Germany. Fluid petrographic analyses were performed on doubly-polished thick sections (100 μm). For each fluid inclusion, the assemblage petrography was carefully documented by optical microscopy (Goldstein & Reynolds, 1994). These fluid inclusion assemblages (FIA) were paragenetically classified as primary (p), pseudo-secondary (ps), secondary (s), isolated inclusions (iso) or clusters of inclusions (refer to Walter *et al.*, 2015, for details). For each analysis, a thrice-repeated heating and freezing cycle was conducted to receive the final dissolution temperature of ice ($T_{m,ice}$) and hydrohalite ($T_{m,hh}$), and the uncorrected homogenization temperature (T_h). For interpretation only, fluid inclusions were used with a minor variability below 0·1°C for $T_{m,ice}$ and $T_{m,hh}$, and below 1°C

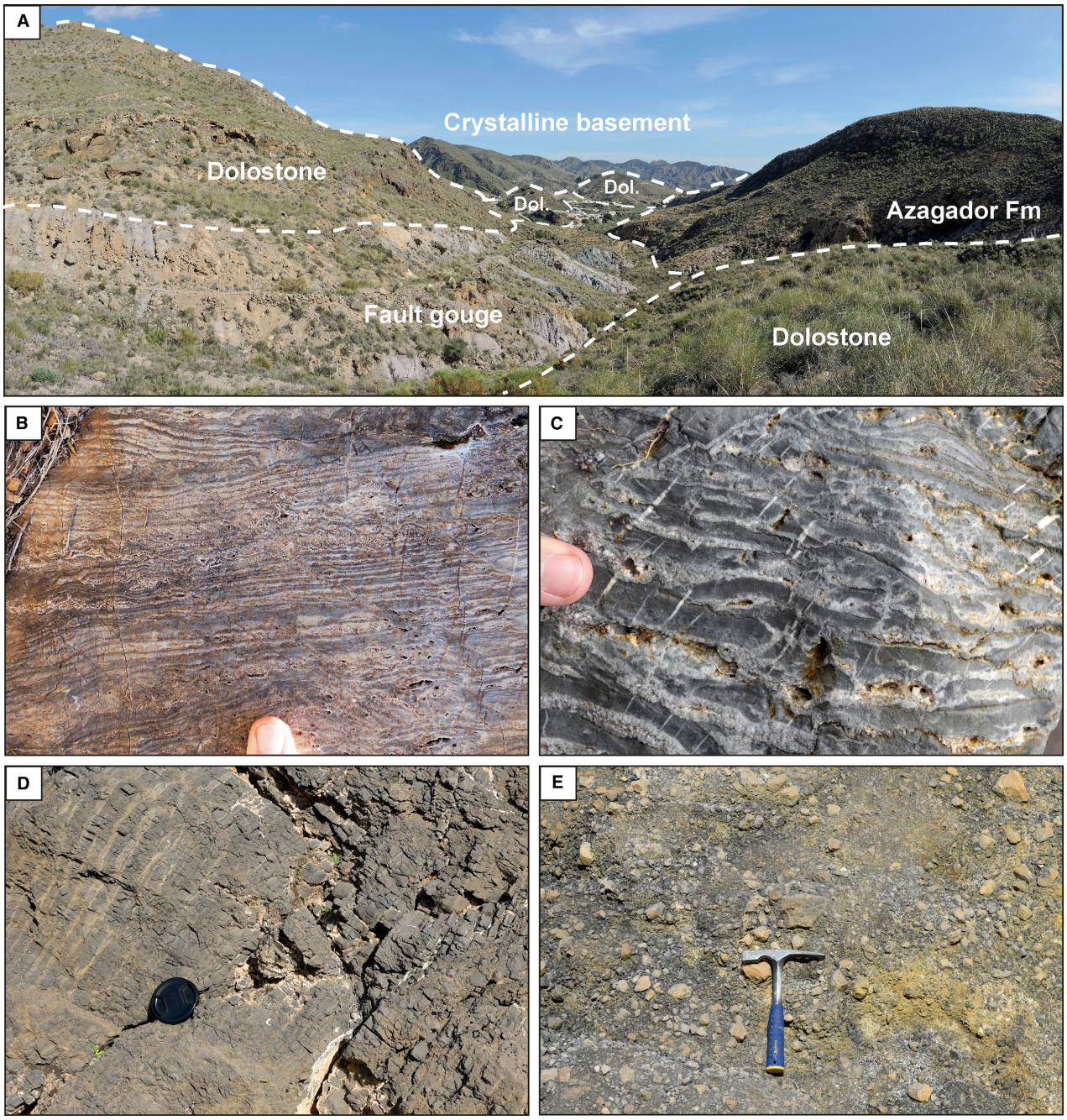

Fig. 5. (A) View to the north-east including 100 m sized blocks of faulted strata floating inside the fault zone. Note the basal autochtonous Neogene Azagador Formation overlying the fault gouge and dolostones. The field of view is *ca* 20 m in the foreground, 150 m for the dolostone block and Neogene formation, and 1000 m in the background (centre). (B) Finely laminated early diagenetic dolostone showing foresets and fining upward features. See finger for scale. (C) Zebra saddle dolomite occurring as a subtype in early diagenetic dolostone is characterized by typical 'ABBA' sequences of millimetre-sized blocky saddle dolomite and early diagenetic dolostone matrix. Note that the zebra dolomite is orthogonally cut by dolomite cement veins. See finger for scale. (D) Brecciated dolostone showing bedding features and some dolomitic cataclasite. Width of the lens cap is 77 mm for scale. (E) Pure cataclastic dolostone with millimetre to centimetre-sized dolostone clasts in cataclasite. See hammer (28 × 19 cm) for scale.

for T_h. Synthetic quartz-hosted H_2O, H_2O–NaCl and H_2O–CO_2 fluid inclusion reference standards (SynFlinc Standard collection) were measured daily for calibration of the stage.

The salinity and molar Ca/(Na + Ca) ratios in the ternary NaCl–$CaCl_2$–H_2O system were quantified by using the MS EXCEL©-based calculation sheet of Steele-MacInnis *et al.* (2011). The volume fraction of each fluid inclusion was estimated based on published volume proportion tables (e.g. Shepherd *et al.*, 1985). The data is presented in volume fraction notation, which illustrates the phase assemblage at room temperature [Lx, numerical subscription refers to the volume percentage of aqueous liquid, vapor (Vx) and solid (Sx)] (Shepherd *et al.*, 1985; Bakker & Diamond, 2006). Pressure correction of the T_h values was quantified using the HOKIEFLINC_-NACL_H2O program of Steele-MacInnis *et al.* (2011), assuming hydrostatic conditions (Delgado *et al.*, 1981; Johnson, 1993; Lonergan & Platt, 1995; Rutter *et al.*, 2012).

Uranium–lead dating of dolomite phases

Four dolomite and two calcite phases were analyzed using the U-Pb small scale isochron dating (UPbSSI) method. The data were acquired from polished sections by laser ablation – sector field – inductively coupled plasma-mass spectrometry (LA–SF–ICPMS) at the Goethe University Frankfurt. A Thermo Scientific Element 2 sector field ICP–MS (Thermo Fisher Scientific, Waltham, MA, USA) was coupled to a RESOLution S-155 (Resonetics, Nashua, NH, USA) 193 nm ArF Excimer laser (CompexPro 102; Coherent, Palo Alto, CA, USA) equipped with a two-volume ablation cell (Laurin Technic, Canberra, Australia). Samples were ablated in a helium atmosphere (0·3 l min^{-1}) and mixed in the ablation funnel with 0·9 l min^{-1} of argon and 0·06 l min^{-1} of nitrogen. Static ablation used a spot size of 213 μm and a fluence of *ca* 1 J cm^{-2} at 15 Hz. Each analysis consisted of 20 sec of background acquisition, followed by 20 sec of sample ablation and 25 sec of washout. Prior to analysis, each spot was pre-ablated for 5 sec to remove any surface contamination. Soda-lime glass SRM-NIST614 was analyzed together with two carbonate reference materials to bracket sample analysis. Analysis spots were set carefully on carbonate domains appearing homogeneous in transmitted light microcopy and on cathodoluminescence images, to avoid or minimize the ablation of contaminants such as clay minerals of detrital origin.

Raw data were corrected offline using a macro-based in-house MS EXCEL© spreadsheet program (Gerdes & Zeh, 2009). Data were plotted in the Tera-Wasserburg diagram and ages calculated as lower intercepts using ISOPLOT 3.71 (Ludwig, 2007). Points of each sample data set derived from a small area (<1 cm^2) and defining linear arrays in the $^{207}Pb/^{206}Pb$ versus $^{238}U/^{206}Pb$ space (Tera-Wasserburg diagram, Tera & Wasserburg, 1972) were interpreted to be a mixture of initial common Pb and Pb that formed due to *in situ* decay of U since mineralization. The age of formation is defined by the lower intercept with the Concordia. See Appendix A1 for a detailed description of the UPbSSI method.

Geochemical analyses

A total of 111 subsamples was extracted using a hand held drill. Those with a mixture of calcite and dolomite were treated with 0·27 m Di-Na-EDTA to dissolve the calcitic phase (Geske *et al.*, 2015b).

The carbon and oxygen isotope values ($\delta^{13}C$ and $\delta^{18}O$) were measured by reacting 0·1 ± 0·01 mg of sample powder with phosphoric acid at a temperature of 70°C. Sample aliquots were measured on a Thermo Finnigan MAT 253 mass spectrometer equipped with a Gasbench II (Thermo Fisher Scientific) and a GC PAL auto sampler (CTC Analytics AG, Zwingen, Switzerland) at the Ruhr-University Bochum. The internal dolomite and calcite standards were calibrated against IAEA-603, CO-1, CO-8 and NBS 18 with a 1σ-reproducibility (SD) of 0·08‰ and 0·06‰, respectively for $\delta^{13}C$, and 0·13‰ and 0·10‰, respectively for $\delta^{18}O$. All values are reported in ‰ Vienna-Pee Dee Formation belemnite (V-PDB) and errors as 1σ SD.

Samples were analyzed for $^{87}Sr/^{86}Sr$ ratios by dissolving a powdered sample containing *ca* 400 ng of Sr (<1 to 10 mg of powder) with 1 ml of 6 M HCl for about 24 h at room temperature. Samples were then dried on a hot plate at 125°C and re-dissolved in 0·4 ml of 3 M HNO_3. The Sr fraction was separated from the matrix using PFA columns filled with TRISKEM ion exchange resin. The samples were flushed with 1 ml of 0·05 M HNO_3 and conditioned with 3 ml of 3 M HNO_3 to remove the matrix. The Sr fraction was then recovered with 2 ml of deionized H_2O. The samples were evaporated on a hot plate at 90°C and then re-dissolved in 1 ml of H_2O_2-HNO_3 (1 : 1) to remove organic remains. After evaporating the samples again on a hot

plate at 60°C and re-dissolving in 0·4 ml of 6 N HCl, they were dried at 90°C. Finally, samples were re-dissolved in 1 µl of ionization-enhancing solution (after Birck, 1986) and loaded on Re single filaments. The loading, column and reagent blanks were <5 pg, <1 ng, and <0·01 ppb, respectively. The $^{87}Sr/^{86}Sr$ ratios were analyzed on a Thermal Ionisation Mass Spectrometer (TIMS) TI-Box (formerly MAT 262; company – Spectromat, Bremen, Germany) at the Ruhr-University Bochum. Long-term reproducibility was determined using the reference materials NIST NBS 987 and USGS EN-1, and resulted in a $^{87}Sr/^{86}Sr$ ratio of 0·710241 ± 0·000002 2σ SE and 0·000032 2σ SD (n = 431) for NIST NBS 987, and a $^{87}Sr/^{86}Sr$ ratio of 0·709159 ± 0·000002 2σ SE and 0·000031 2σ SD (n = 377) for USGS EN-1. Errors of $^{87}Sr/^{86}Sr$ ratios are reported in 2σ SE. A similar analytical technique is described by Faure & Powell (1972).

RESULTS

Based on field observations, three types of Alpujarride dolostones, from least to most altered, were recognized: (i) Intact, finely (millimetre-sized) laminated, early diagenetic dolomitized grainstones with preserved lamination, ripple foresets and fining-upward cycles (Fig. 5B). Dolo-grainstones are also characterized by blocky zebra saddle dolomite (Fig. 5C), which formed bedding-parallel or along cleavage planes, and are typically accompanied by stylolites. Zebra dolomites were recently interpreted to form during burial by dissolution-void creation within sedimentary laminations, resulting in an 'ABBA' sequence (A – recrystallized host rock; B – white saddle dolomite; Vandeginste *et al.*, 2005). Zebra dolomite is common in the Alpujarride dolostones, and known from other localities in the Betic Cordilleras (e.g. Sanz de Galdeano & López Garrido, 2014). For more details on zebra dolomite fabrics see Vandeginste *et al.* (2005), Morrow (2014) or Wallace & Hood (2018), and references therein. (ii) Partially to fully brecciated dolomitized grainstones with variable degrees of clast fitting (Fig. 5D). Carbonate cements locally form the host carbonate in which clasts are embedded. Bedding features may be preserved within individual clasts but are commonly broken up, and the space between clasts is occluded by a matrix of dolomitic cataclasite. (iii) Dolomitic cataclasite (i.e. fault gouge), with millimetre to centimetre-sized dolostone clasts (Fig. 5E). All sedimentary features are overprinted and disintegrated. Evidence of hydrothermal alteration of the cataclasite facies includes its brown-yellow colouration. In the north-western study area, dolostones are present as strongly-altered iron-manganese ores, previously mined over the last century.

Petrography and paragenetic succession

A paragenetic succession of the Alpujarride dolostones has been established from field observations (Fig. 5), thin section data and cathodoluminescence analysis (Figs 6 and 7; Table 1). Only the most significant features are reported here, but additional material can be found in the Appendix A1. Dolomite terminology is after Sibley & Gregg (1987). Eight dolomite cements are present: Dol 1, recrystallized early diagenetic, fine to coarse crystalline planar-s dolomite (Figs 6A to D and 7); Dol 2, saddle dolomite cements characterized by curved crystal surfaces and sweeping extinction forming coarse crystalline nonplanar dolomite (Figs 6 and 7A to D); Dol 3, volumetrically less significant fine to medium crystalline nonplanar dolomite (Fig. 6E and F); Dol 4, fine crystalline nonplanar dolomite (Figs 6A, 6B, 6E to H, 7A and 7B); Dol 5, fine to coarse crystalline nonplanar to planar-s dolomite (Figs 6 and 7); Dol 6, fine crystalline nonplanar dolomite (Appendix A1; Fig. A1E and F); Dol 7, fine to coarse crystalline nonplanar to planar-s dolomite (Figs 6E, 6F and 7); and Dol 8, medium to coarse crystalline nonplanar dolomite (Fig. 6E to H). The paragenetically-youngest dolomitic material is present in the form of a cataclasite (C 1) (Fig. 7G and H), which does not qualify as a diagenetic phase, but as a tectonic product. This cataclasite consists of crushed (micron-sized) crystals of the eight dolomite phases. Latest stage calcitic cements (LMC 1 to LMC 4, Figs 6E to H, 7C and 7D; and HMC 1 to HMC 3, Fig. 6E to H) and authigenic quartz (characterized by intrinsic dark blue luminescence) do not occur in a defined order of precipitation, but were placed into context based on appearance. In contrast, Malaguide dolostones generally consist of fine to medium crystalline planar-e to planar-s dolomite containing well-preserved and recrystallized ooids.

Two sets of stylolites occur in the Alpujarride dolostones: Type 1 stylolites (S1) formed

between layers of different grain size in the Dol 1 early diagenetic dolostone, and are often cut by paragenetically younger Dol 5 or Dol 7 cements (Fig. 7A and B); Type 2 stylolites (S2) formed after the Dol 1 early diagenetic dolostone and the Dol 2 zebra saddle dolomite, and are cut by veins infilled by Dol 5 or Dol 7 cements (Fig. 6C and D). The dolostones have a low porosity, as most pore space has been occluded by dolomite and calcite cements.

Microthermometry

A classification was made to place the fluid inclusions into temporal context (Fig. 8A to C). Primary inclusions with irregular and angular shapes with dimensions of <10 μm occur along crystal growth zones. Secondary fluid inclusions post-date the whole paragenetic assemblage, whereas pseudo-secondary inclusions are related to healed cracks and often pre-date primary fluid inclusions of the next dolomite generation.

Two types of fluids were recognized (Figs 8 and 9): The first fluid type occurs in primary inclusions and fluid inclusion clusters, with both inclusion types common in Dol 1, 2, 4, 5, 7 and 8. These record the first melting point in the binary NaCl–H_2O system, with a eutectic temperature at −21·2°C (Fig. 9, eutectic 2). Ice occurs as the last dissolving phase whereas hydrohalite dissolves at the binary eutectic. The calculated final melting temperature of ice is between −2·8°C and −19·3°C, resulting in calculated salinities from 4·7 to 21·9 wt.% $NaCl_{eq}$. Data are scattered over a wide range, but if looking at a specific position in the paragenetic sequence, defined clusters are observed. With progressing temporal evolution, the salinity of diagenetic fluids increases. Uncorrected homogenization temperatures vary between 45°C and 230°C, and also increase within the paragenetic sequence. Within a defined fluid inclusion assemblage, salinity and T_h are nearly constant, but typically vary between assemblages. The inclusions contain volume fractions of *ca* $L_{90}V_{10}$ to $L_{95}V_5$.

The second fluid type (only in sdol 8) is classified as H_2O–NaCl–$CaCl_2$ fluid with a characteristic first melting point around the ternary eutectic at −52·0°C (Fig. 9, eutectic 1). These inclusions are present in secondary cavities of healed fractures in dolomite phase Dol 8. The last melting temperature of ice is between −14·1°C and −20·3°C, whereas hydrohalite dissolves between −24·0°C and −26·0°C, resulting in a salinity of 21·1 to 22·0 wt.% NaCl + $CaCl_2$. The inclusions contain volume fractions of about $L_{90}V_{10}$. Micro Raman Spectroscopy analyses of this type failed due to the subcritically-small size of the inclusions.

Uranium–lead age data of dolomite phases

Dolomite phases range in $^{207}Pb/^{206}Pb$ values from 0·541 to 0·835, and in $^{238}U/^{206}Pb$ values from 0·39 to 13·57. In the Tera-Wasserburg diagram, this results in lower intercept ages of 175·0 ± 11·0 Ma, 186·1 ± 8·0 Ma and 186·4 ± 5·6 Ma using initial $^{207}Pb/^{206}Pb$ values of 0·841 to 0·850 (Fig. 10). Based on scanning electron, cathodoluminescence and transmitted light microscopy, no evidence for uranium minerals was recognized in any of the samples. The U-Pb dolomite ages record recrystallization and mineralization between the Early and Middle Jurassic (164·0 to 194·1 Ma). The ages of both early diagenetic Dol 1 and zebra saddle Dol 2 were indistinguishable. Cement phases Dol 5 and Dol 7, and LMC 2/LMC 3 were not datable due to low U concentration and a Pb concentration that is too high, respectively.

Fig. 6. Transmitted light images placed against cathodoluminescence properties of different paragenetic phases in early diagenetic dolostone facies. (A) and (B) Recrystallized, patchy luminescent early diagenetic dolostone (Dol 1) with zebra saddle dolomite (Dol 2) filled pores. Note distinctive inclusion-rich saddle dolomite (Dol 4) overgrown by less inclusion-rich saddle dolomite (Dol 5). (C) and (D) S2 stylolite intersects early diagenetic dolostone (Dol 1) and zebra saddle dolomite (Dol 2). Note numerous veins filled by Dol 5. (E) and (F) Zebra saddle dolomite pore including almost all dolomitic cements of the paragenetic sequence. The non-luminescent Dol 3 is partly corroded. Note the patchy luminescence of Dol 2 to Dol 7, and the characteristic curved crystal faces of saddle dolomite phases. Dol 5 and Dol 7 occur as syntaxially grown saddle dolomite in small veins. (G) and (H) Zebra dolomite pore filled by complex sequence of late meteoric/vadose cements. For interpretation of the references to colour in this figure legend, the reader is referred to the online version of this article.

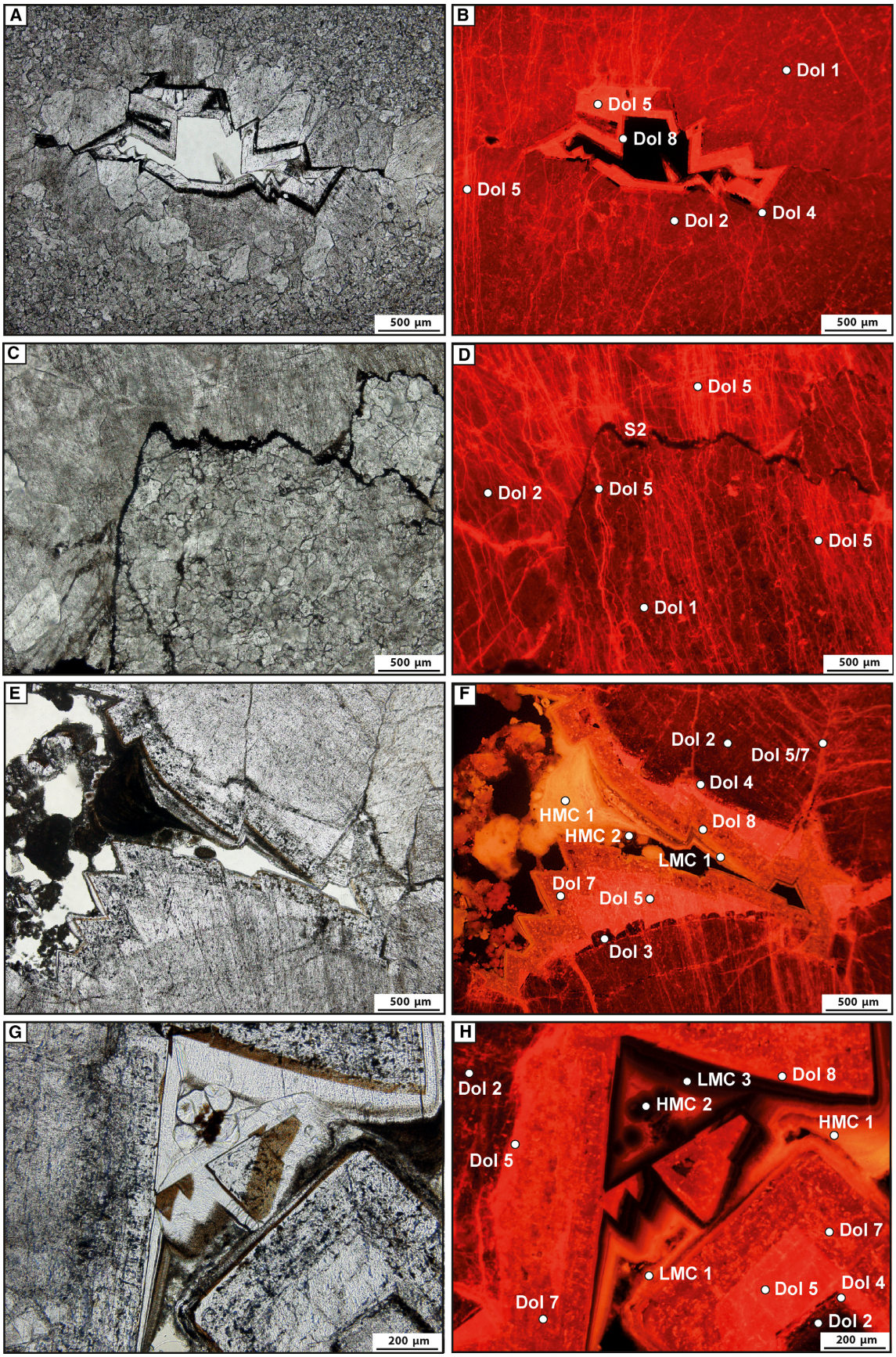

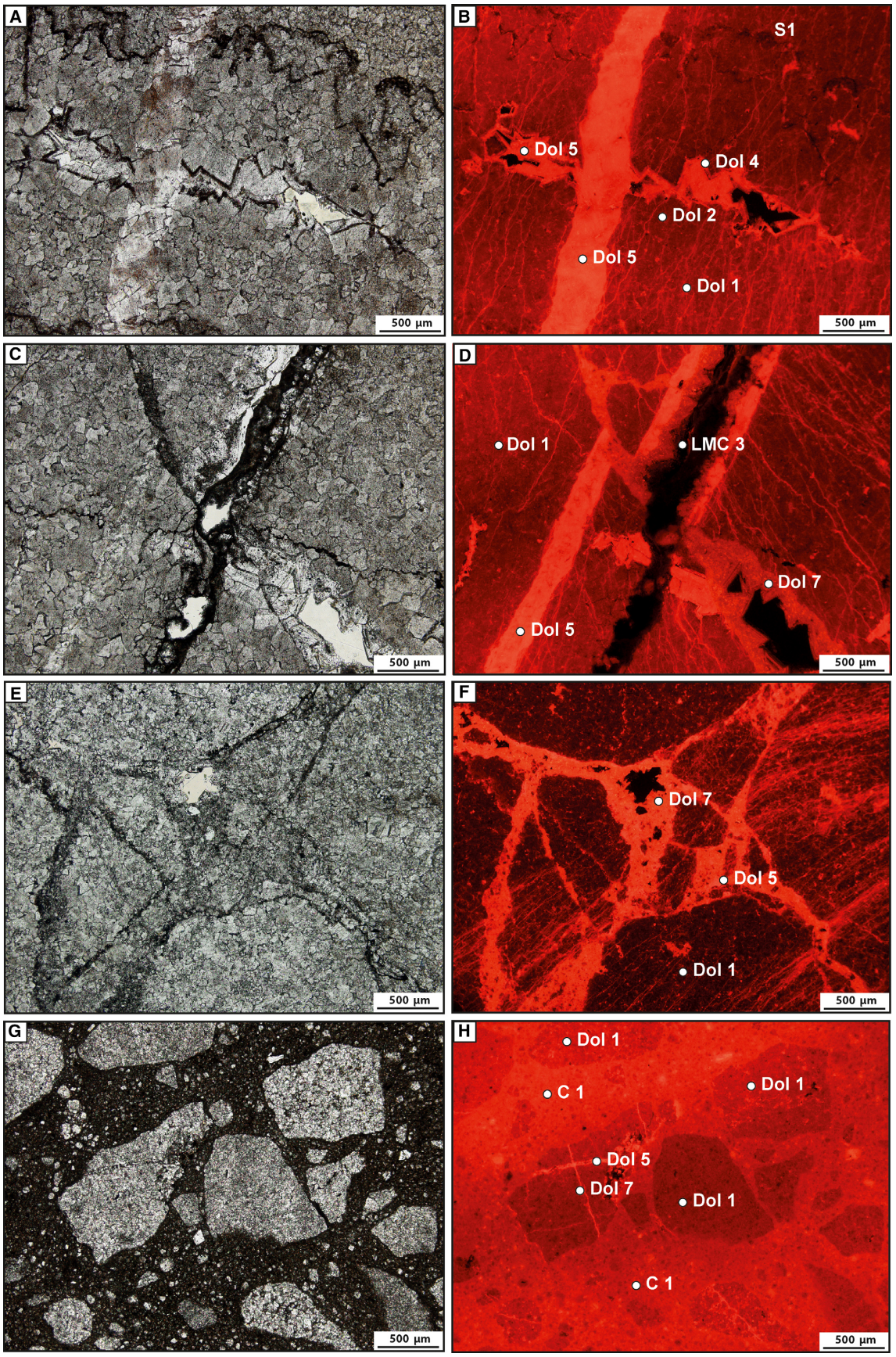

Isotope and elemental geochemistry

Stable $\delta^{13}C$ and $\delta^{18}O$ isotope values and $^{87}Sr/^{86}Sr$ ratios for all drilled cement phases are given in Table 1, where only the most important features are reported. Detailed tables including: (i) major and trace element concentrations; and (ii) $\delta^{13}C$ and $\delta^{18}O$ ranges, and $^{87}Sr/^{86}Sr$ in sample groups, are given in the Appendix A1 (Table A1A and B, and Table A2, respectively). Dolomite $\delta^{13}C$ and $\delta^{18}O$ values are shown in three clusters representing an increasing degree of brecciation and overprint of dolostones as previously described.

The $\delta^{18}O$ values of 111 powder samples range from −8·4‰ (early diagenetic dolostone clasts in cataclasite) to +0·7‰ (Malaguide dolostone), independent of mineralogy and age of formation. Among these, Alpujarride dolomite phases yield $\delta^{18}O$ values from −8·4 to −4·3‰ (mean of −6·3‰; n = 72). Early diagenetic dolostone samples have a $\delta^{18}O_{mean}$ value of −7·0‰ (n = 24). Clasts of early diagenetic dolostone in a cataclastic matrix have a $\delta^{18}O_{mean}$ value of −5·0‰ (n = 10; all dolomite types in fault gouge $\delta^{18}O_{mean}$ = −5·3‰, n = 8) and are enriched in ^{18}O relative to other early diagenetic dolostones. Malaguide dolostones range from −3·2 to +0·7‰ (mean of −1·1‰; n = 14). Neogene carbonate $\delta^{18}O$ values vary between −3·6‰ (Neogene matrix micrite in autochthonous units, n = 6) and −0·4‰ (Neogene bivalve, n = 2).

The $\delta^{13}C$ values of all samples range from −9·9‰ (meteoric low-Mg calcite) to +2·5‰ (Malaguide dolostone). Among the Alpujarride dolomite phases, $\delta^{13}C$ values range from −1·7‰ (dolomite 4 to 8) to +2·3‰ (zebra saddle dolomite 2), with a mean $\delta^{13}C$ value of +0·9‰ (n = 72). Malaguide dolostones range from −0·6 to +2·5‰, with a mean value of +0·9‰ (n = 14). Autothonous Neogene calcitic units from the adjacent Carboneras Nijar Basin range from −3‰ in very porous, argillaceous limestones (LSTs) of the Azagador Formation, to +0·5‰ in a bivalve shell. Low-Mg calcite cements and calcitic caliche (i.e. subrecent soil carbonates), have comparably ^{13}C-depleted values compared to the dolomite phases, with means of −8·3‰ (n = 5) and −8·2‰ (n = 4), respectively.

The strontium isotope ratios (n = 51, Table 1) range between 0·706022 ± 0·000004 (speleothems collected at the surface) and 0·710737 ± 0·000005 (LMC 2 and LMC 3). The mean $^{87}Sr/^{86}Sr$ ratio of all Dol 1 early diagenetic dolostones is 0·708311 ± 0·000005 (n = 4). The mean $^{87}Sr/^{86}Sr$ ratio is 0·708689 ± 0·000055 (n = 2) for C 1 brecciated dolostones and 0·709031 ± 0·000047 (n = 3) for C 1 cataclastic dolostones. There is a general trend towards lower values from type 1 early diagenetic dolostone to the increasingly radiogenic composition of cataclasite.

INTERPRETATION AND DISCUSSION

The paragenetic succession of the dolostones is presented and discussed below within genetic and temporal context. The interpretation and discussion of these rocks commences with the deposition of Anisian–Rhaetian (247 to 201 Ma) precursor carbonates in a platform environment, and culminates in Holocene meteoric diagenesis of the exhumed Carboneras Fault Zone and the related lithologies.

Paragenetic sequence

The complex paragenetic succession of dolostones in the Carboneras Fault Zone is composed of bulk replacement dolostones (dolomicrites Dol 1) with calcitic and aragonitic precursors (Fig. 11). These dolostones experienced a series of subsequent dissolution–reprecipitation phases during intermediate burial, resulting in the opening of bedding-parallel

Fig. 7. Transmitted light images compared to cathodoluminescence properties of different paragenetic phases, transitioning from early diagenetic towards cataclastic dolostone facies. (A) and (B) Recrystallized, patchy luminescent early diagenetic dolostone (Dol 1) with zebra saddle dolomite (Dol 2) filled pore and S1 stylolite separating a fine-grained from a coarse-grained layer. Note the bedding-perpendicular vein, cutting the stylolite and zebra saddle dolomite pore. (C) and (D) Faulted Dol 5 vein overgrown by Dol 7 saddle dolomite in patchy luminescent Dol 1 early diagenetic dolostone. Open fractures are partly filled by LMC 3. (E) and (F) Recrystallized, patchy luminescent brecciated dolostone containing cataclastic C 1 matrix dominated by Dol 7 cement and partly crushed early diagenetic dolostone. (G) and (H) Endmember cataclastic dolostone with μm-to-mm-sized fragments of Dol 1 early diagenetic dolostone in pure C 1 cataclastic dolostone matrix. For interpretation of the references to colour in this figure legend, the reader is referred to the online version of this article.

Table 1. Paragenetic sequence (starting with Dol 1 and ending with HMC 3) of Carboneras dolostones plotted against phase specific petrography, characteristic features, crystal size, volumetric significance, luminescence colour, and their carbon, oxygen and strontium isotope composition. Additional geochemical data for individual samples and groups is given in the Appendix A1.

Phase	Petrography	Characteristic features	Crystal size	Volumetric significance	Luminescence	$\delta^{13}C$ (‰) min./max./mean	$\delta^{18}O$ (‰) min./max./mean	$^{87}Sr/^{86}Sr$ (± 2 σ) min.	max.
HMC 3		Internally layered, pendant, drop-shaped, inclusion rich	Crypto- to micro-crystalline	Low	Dark red				
HMC 2		Forms botryoidal-shaped fibrous aggregates	Microcrystalline	Very low	Bright orange to yellow	−1·5/1·1/−0·1	−3·7/−2·9/−3·2	0·708855 (6)	0·708884 (5)
HMC 1		Internally layered, pendant, drop-shaped	Crypto- to micro-crystalline	Low	Bright orange to yellow				
LMC 4	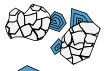	Zoned blocky crystals	Macrocrystalline	Low	Non-luminescent to yellow				
Qz 2		Authigenic, idiomorphic to hypidiomorphic	Micro- to macro-crystalline	Very low	Non-luminescent	Not applicable			
LMC 3		Zoned blocky crystals	Macrocrystalline	Low	Non-luminescent to dark orange	−9·9/−6·6/−8·3	−6·7/4·6/−5·7	0·709435 (5)	0·710737 (5)
LMC 2		Inclusion rich	Macrocrystalline	Low	Dark red and patchy				
LMC 1		Consistently appears as thin layer	Cryptocrystalline	Very low	Bright orange				
Qz 1		Authigenic, idiomorphic to xenomorphic	Micro- to macro-crystalline	Very low	Non-luminescent	Not applicable			
C 1	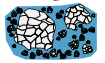	Cataclasite consisting of crypto-macrocrystalline dolomitic rock fragments of Dol 1-8	Not forming crystals	Very high	Bright orange	0·0/1·0/0·5	−6·7/−4·3/−5·3	0·708649 (5)	0·709218 (5)
Dol 8		Brown in transmitted light, consistently occurs as thin layer in Dol 2 pores	Micro- to macro-crystalline	Very low	Bright orange				
Dol 7	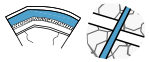	Curved crystal faces, sweeping extinction, often in Dol 2 pores and veins which overgrow or cut Dol 5	Macrocrystalline	High	Intense orange and patchy				
Dol 6		Inclusion rich, often corroded or absent	Microcrystalline	Low	Bright orange and patchy	−1·7/1·7/0·3	−7·8/−6·0/−6·6	0·708318 (5)	0·708840 (5)
Dol 5		Curved crystal faces, sweeping extinction, common in Dol 2 pores and veins which cut lamination	Macrocrystalline	High	Bright orange-red and patchy	−0·7/0·0/0·7	−7·4/−6·4/−7·0	0·708270 (5)	0·708569 (6)
Dol 4		Very inclusion rich, often corroded, black in transmitted light, consistently occurs as thin layer	Micro- to macro-crystalline	Very low	Bright orange and patchy				
Dol 3		Iron-rich, often corroded or absent	Macrocrystalline	Very low	Non-luminescent and patchy	No data	No data	No data	
Dol 2		Curved crystal faces, sweeping extinction, fascicular-optic dolomite	Macrocrystalline up to 10mm	High	Dark red and patchy	0·5/2·3/1·3	−7·9/−6·5/−7·3	0·708076 (5)	0·708700 (5)
Dol 1	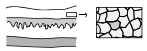	Recrystallized early diagenetic dolostone	Micro- to macro-crystalline	Very high	Red to dark orange and patchy	0·7/1·8/1·2	−8·4/−0·5/−6·1	0·707603 (6)	0·708789 (5)

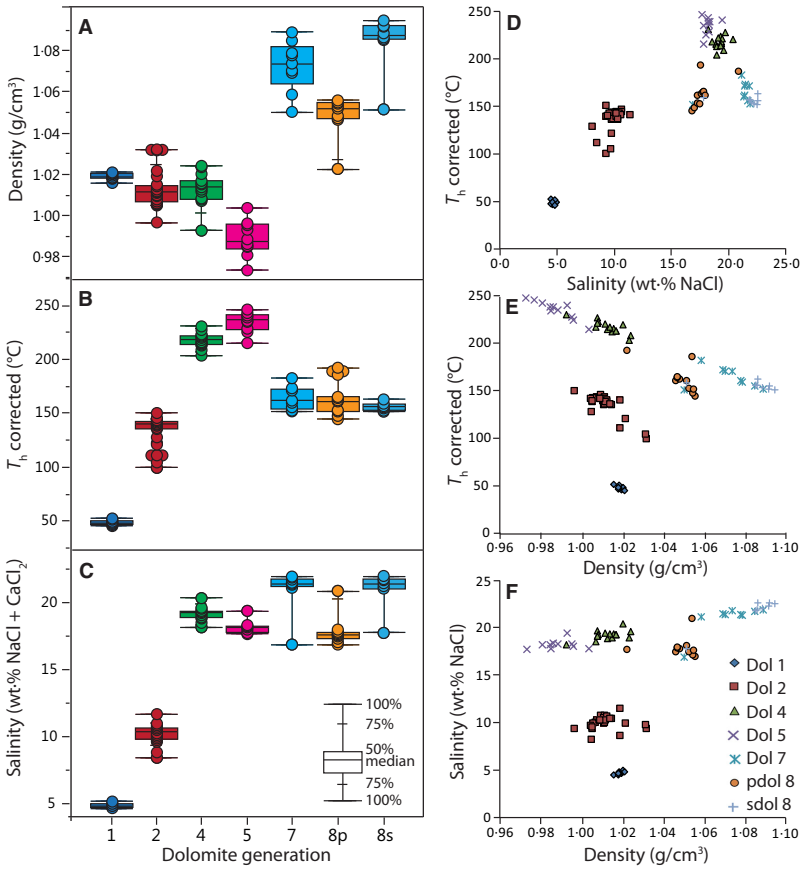

Fig. 8. Homogenization temperatures, fluid salinity, and density in cement phases Dol 1, 2, 4, 5, 7 and 8. Boxplots show dolomite generations plotted from the bottom towards the top versus (A) salinity (wt.% NaCl + $CaCl_2$), (B) corrected homogenization temperatures (T_h) and (C) bulk fluid density (g cm^{-3}). (D) Fluid salinity versus homogenization temperatures. (E) Fluid density (g cm^{-3}) versus homogenization temperatures. (F) Fluid density (g cm^{-3}) versus fluid salinity (wt.% NaCl). For interpretation of the references to colour in this figure legend, the reader is referred to the online version of this article.

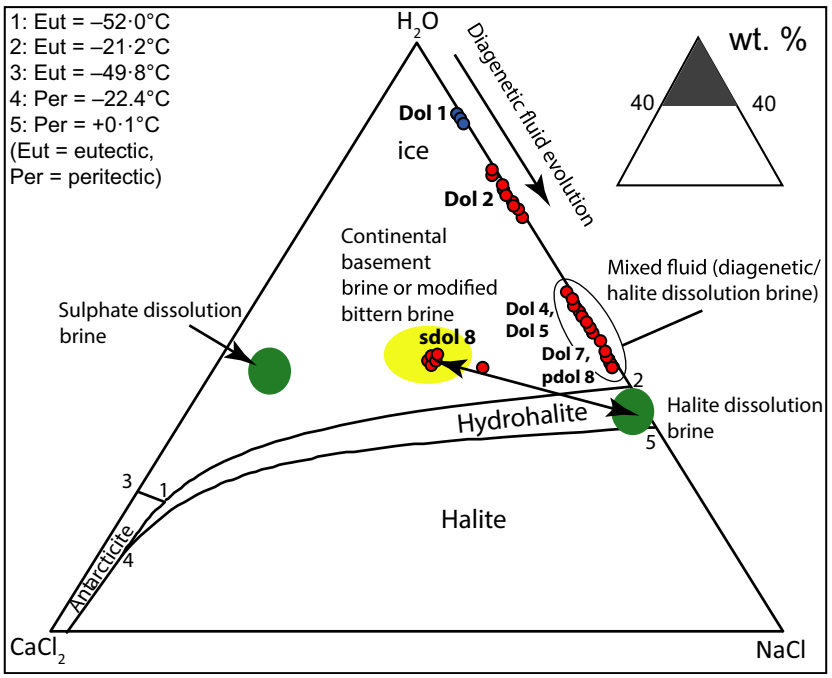

Fig. 9. Fluid salinity in cement phases Dol 1, 2, 4, 5, 7 and 8. Microthermometric results in the ternary H_2O–NaCl–$CaCl_2$ phase diagram. For interpretation of the references to colour in this figure legend, the reader is referred to the online version of this article.

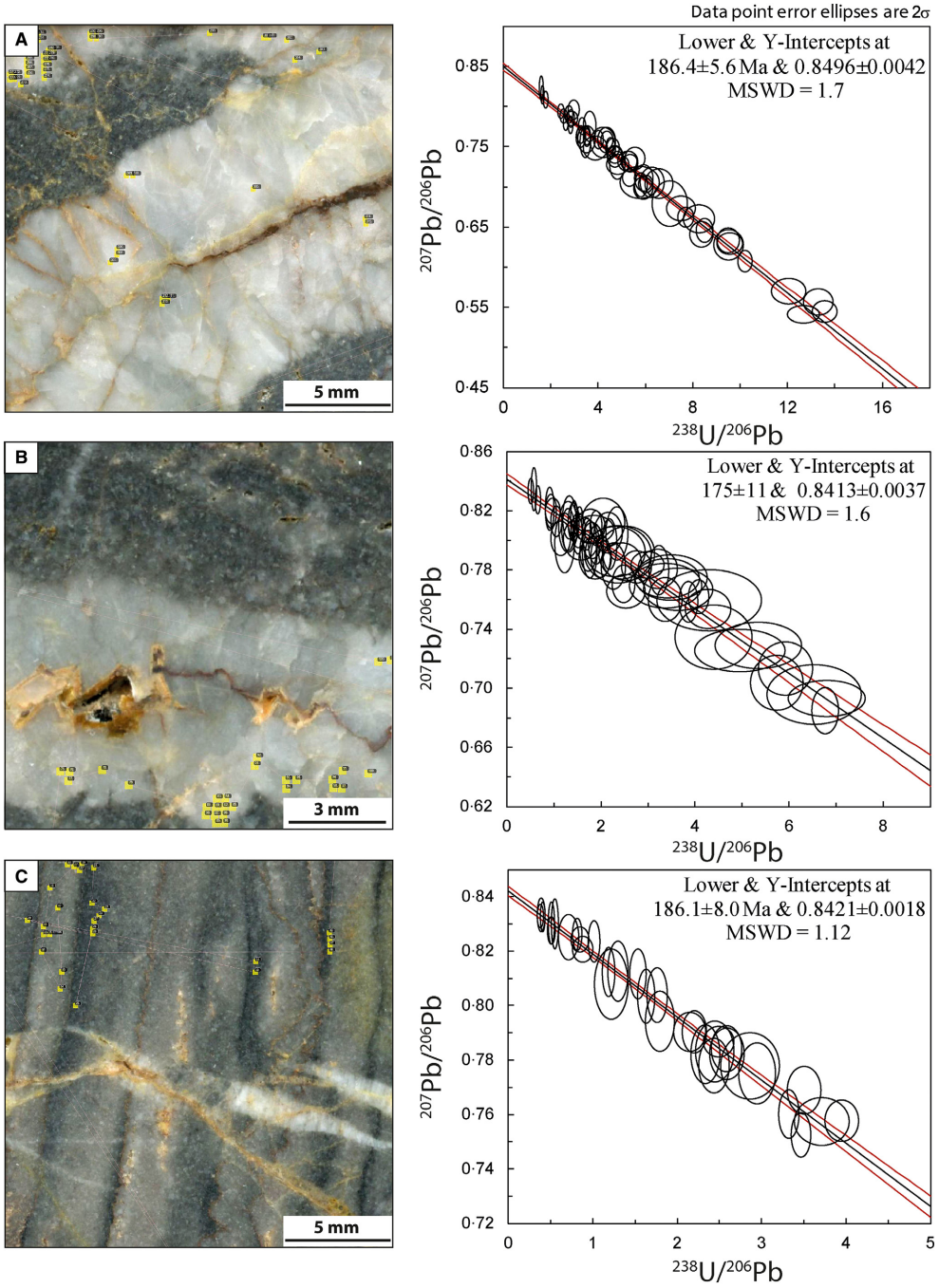

Fig. 10. Sample images including analyzed spots and the respective Tera-Wasserburg diagram to illustrate the UPbSSI results for selected locations. All ages are lower intercept ages: (A) Zebra saddle dolomite Dol 2. (B) Zebra saddle dolomite Dol 2 from the same section in which petrographic images of Fig. 6E to H were taken. (C) Early diagenetic dolostone Dol 1 from homogeneous lamination interval shown in Fig. 12. MSWD, mean square weighted deviation.

elongated voids (i.e. 'zebra' fabrics; Vandeginste *et al.*, 2005; Morrow, 2014; Wallace & Hood, 2018), which were occluded by saddle dolomite (zebra saddle Dol 2; Figs 5C, 10A, 10B and 11). Zebra fabrics and elevated fluid inclusion homogenization temperatures indicate a dissolution-void-creating origin of the voids and saddle dolomite precipitation from hydrothermal formation fluid during burial (Radke & Mathis, 1980; Wallace & Hood,

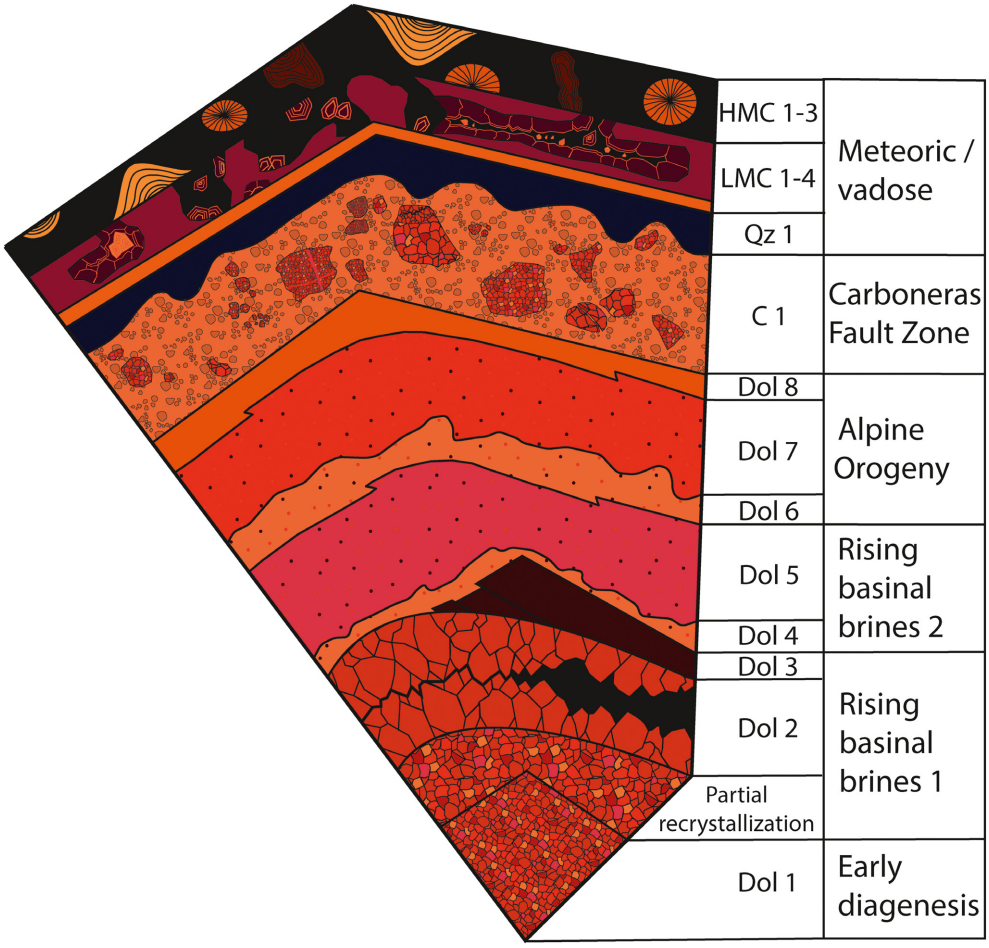

Fig. 11. Complete paragenetic sequence of diagenetic phases with typical cathodoluminescence colours related to their diagenetic and tectonic environment of precipitation or formation. Remaining pore space is marked in black.

2018). Partial corrosion of Dol 3 cements (Figs 6F and 11) suggests a change in fluid chemistry towards acidic composition. Dolomite cements Dol 4 and Dol 5 are characterized by high fluid inclusion homogenization temperatures up to 250°C (Fig. 8B, D and E); Dol 5 precipitated in bedding-perpendicular veins that cut through the zebra dolomite, Dol 2 (Fig. 7B). The sigmoidal morphology of the Dol 5 subcrystals evidences growth under shear stress during vein opening. The inclusion-rich Dol 6 indicate either another change in fluid composition, or a precipitation hiatus. This is evidenced by decreased fluid inclusion temperatures (215 to 250°C in Dol 5 versus 150 to 180°C in Dol 7, Fig. 8B, D and E). The late diagenetic dolomite cements (Dol 7 and Dol 8) occur in fractures cross-cutting paragenetically-older cement phases, occluding porosity around breccia clasts, or overgrow saddle dolomite cements (Dol 2). Petrographic evidence suggests that the Dol 5 veins were reactivated and widened during tectonic activity, to allow space for the precipitation of Dol 7 and Dol 8 cement phases; Dol 7 and 8 represent the final precipitation of dolomite. Subsequent activation of the Carboneras Fault Zone led to the formation of the dolomitic cataclasite (C 1; Fig. 11), followed by late-stage (meteoric) authigenic quartz (Qz 1; Fig. 11) and calcite cementation (LMC 1 to LMC 4, HMC 1 to HMC 3; Fig. 11). Below, this paragenetic sequence is discussed in context.

Evolution of a complex dolostone archive

Protolith deposition and early marine diagenetic dolomitization

The precursor carbonates of the dolostones were deposited on a large (*ca* 400 km in an east–west direction) Anisian–Rhaetian carbonate platform,

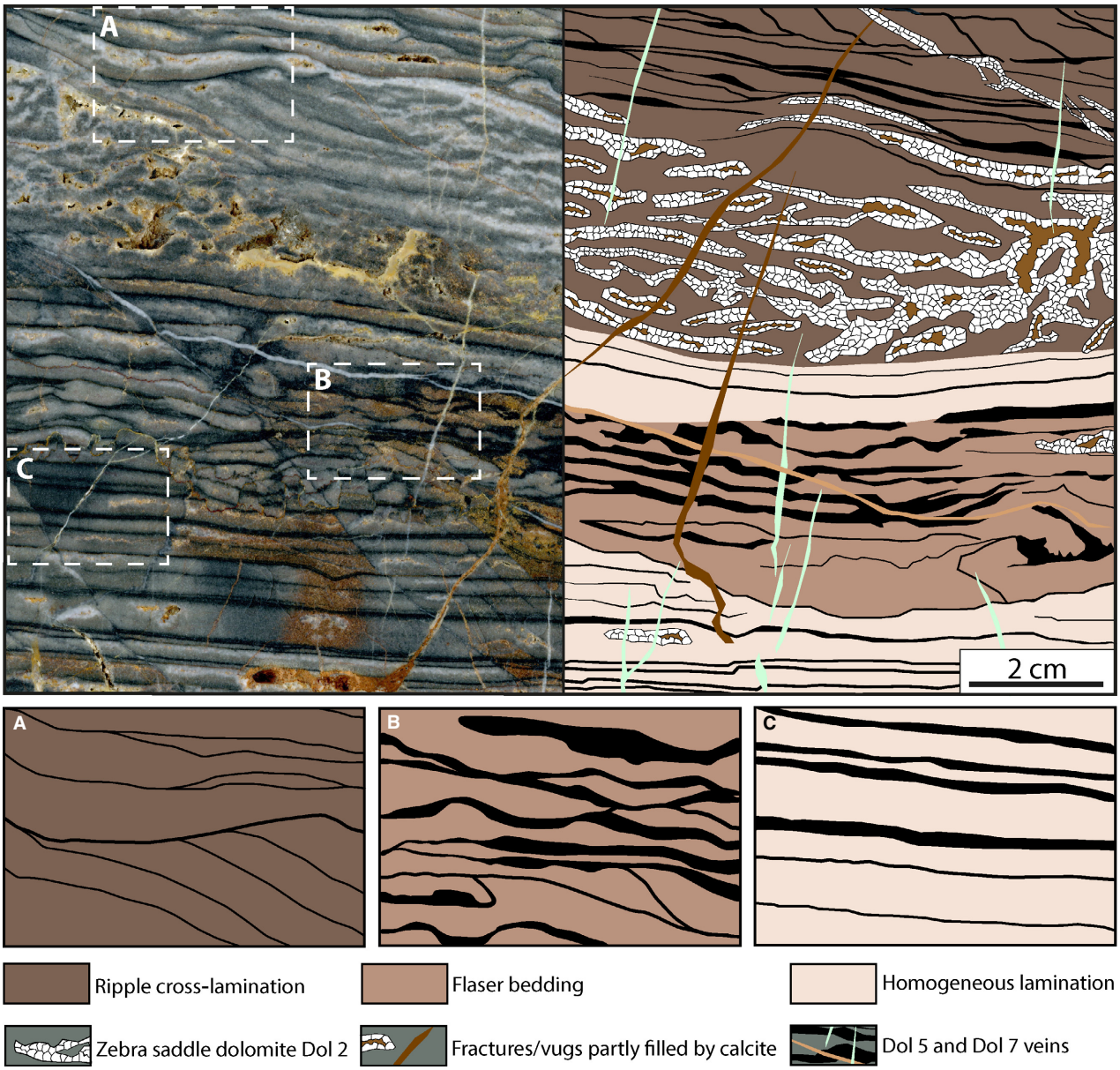

Fig. 12. Well-preserved sedimentary structures in Middle/Late Triassic early diagenetic dolostones (Dol 1) from the Carboneras Fault Zone. Re-drafted sedimentary features on the right correspond to the features observed on a polished slab of early diagenetic Dol 1 dolostone on the left. (A) Ripple cross-lamination. (B) Flaser bedding. (C) Homogeneous lamination of fine-grained (dark) and course-grained (bright) dolostone layers.

likely belonging to the opening Proto-Atlantic region (Delgado *et al.*, 1981; Martín & Braga, 1987). Well-preserved sedimentary features (Fig. 12) of the precursor laminar tidal flat facies (Martín & Braga, 1987) include flaser bedding and ripple cross-lamination (Fig. 12A to C). This preservation suggests an early diagenetic, fabric-preserving replacement dolomitization. Low reconstructed fluid temperatures (median of 50°C) in preserved dolomite rhombs from the later recrystallized Dol 1 further imply shallow burial dolomitization. Fluid inclusion salinity of 5 wt.% NaCl, in the absence of $CaCl_2$, indicates a modified seawater parent fluid (i.e. moderately saline brines) (Fig. 8C, D and F). Dolomitized Middle Triassic barrier-island facies to the west of the study area were similarly interpreted as the product of early reflux dolomitization (Martín, 1978). This interpretation is strengthened by the absence of calcite cement formation,

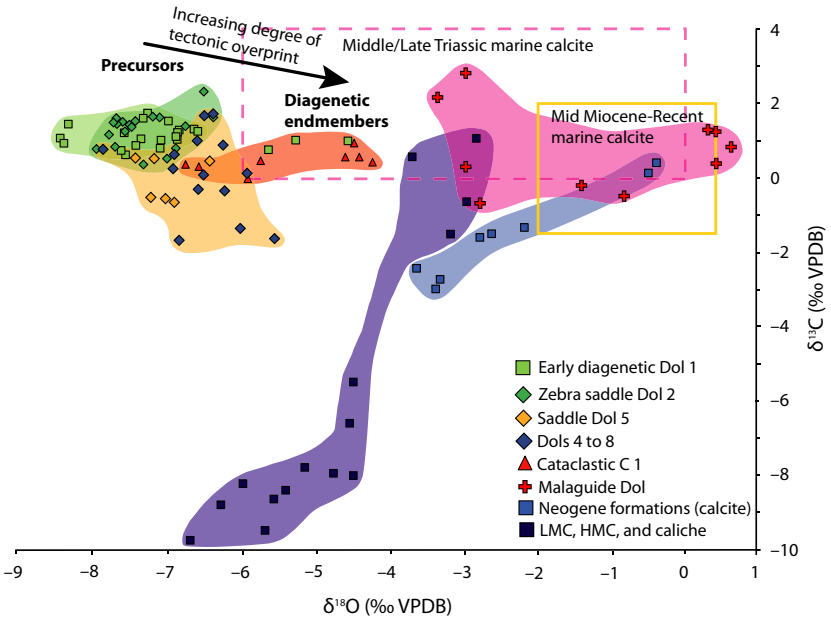

Fig. 13. Cross-plot of $\delta^{18}O$ and $\delta^{13}C$ data for all analyzed samples of dolomite and calcite phases. The stable isotopic composition of Middle Miocene to Recent and Middle/Late Triassic marine calcite (derived from shallow water tropical/subtropical marine calcite) are indicated in the yellow and stippled purple boxes (from Grossman, 2012; Saltzman & Thomas, 2012; Veizer & Prokoph, 2015). The annotated trend indicates a shift in $\delta^{18}O$ of +4‰ from dolomitic precursor phases towards the cataclasite diagenetic end member with increasing degree of tectonic overprint. VPDB, Vienna-Pee Dee Formation belemnite.

possibly due to previous detachment of Ca-ions during ordering of the Dol 1 crystal structure driven by tidal pumping or convection cells in the platform.

Carbon isotope ($\delta^{13}C$) values of fine crystalline dolomicrite Dol 1 (0·7 to 1·8‰) remain within the range of their Middle/Late Triassic marine formation fluids (*ca* 0 to 4‰) (Fig. 13). In contrast, oxygen isotope ($\delta^{18}O$) data of Dol 1 were shifted towards more negative values (−6·5 to −8·0‰), and therefore do not preserve the early diagenetic dolomitization signature of Middle/Late Triassic marine fluids (*ca* −6 to 0‰). Fluid inclusion data suggest that strongly evaporative marine porewaters, typically resulting in a positive shift in $\delta^{18}O$ values, were not present (Fig. 8A to E). Fractionation during LST to dolostone neomorphosis (at Earth surface temperatures) is also expected to cause a positive shift in $\delta^{18}O$ values (Swart, 2015). Cathodoluminescence data help to explain the unexpectedly low $\delta^{18}O$ values observed. The patchy luminescence of Dol 1 indicates partial recrystallization of the early diagenetic dolomite phase (Fig. 11). Numerous bright luminescent fissures cross-cut the Dol 1 matrix and suggest influence of a significantly deeper burial fluid (Fig. 6B). This fluid–rock interaction may have resulted in the resetting of the fluid-buffered oxygen isotope, but not the rock-buffered carbon isotopes (Fig. 13). Furthermore, a different mechanism to explain the lowering of $\delta^{18}O$ values could be early meteoric overprint of the dolostones (Lohmann, 1987); however, this seems unlikely due to the absence of meteoric vadose or phreatic textures.

Intermediate burial and hot hydrothermal overprint

Zebra saddle dolomite Dol 2 (Figs 5C, 10A, 10B, 11 and 12) is characterized by $\delta^{13}C$ and $\delta^{18}O$ values similar to the early diagenetic Dol 1 phase (Dol 2_{mean} = $\delta^{13}C$ 1·3‰, $\delta^{18}O$ −7·3‰, n = 21; Fig. 13). Wallace & Hood (2018) suggested that if zebra dolomites and their host rock dolostone share a similar oxygen and carbon composition, then precipitation from the same parent fluid may be assumed. This may in part be true, because the two phases have similar U-Pb ages (Dol 1 = 186·1 ± 8·0 Ma, Dol 2 = 186·4 ±5·6 Ma and 175·0 ± 11·0 Ma). However, significantly different fluid inclusion

homogenization temperatures and salinities between Dol 1 and Dol 2 (45 to 52°C versus 100 to 150°C, and 5 versus 11 wt.% NaCl, respectively; Figs 8 and 9) support a different scenario. These data suggest the precipitation of Dol 1 in early diagenetic shallow marine burial conditions, and a significantly later (tens of Myr) hydrothermal precipitation of Dol 2. Along with the structural evidence and higher salinity, fluctuating fluid inclusion temperatures are characteristic for hydrothermal dolomite cements including zebra dolomite (Wilson *et al.*, 1990; Morrow, 2014), further supporting the hypothesis of different formation fluids of Dol 1 and Dol 2. Early diagenetic Dol 1 recrystallized, and therefore bears similar $\delta^{13}C$ and $\delta^{18}O$ values as Dol 2. However, some of the primary fluid inclusions from Dol 1 remained intact in non-recrystallized dolomite rhombs, preserving the initial signature of Dol 1 fluids. Precipitation of the zebra saddle dolomite (Dol 2) may have occurred after the recrystallization of Dol 1, as S1 stylolites post-date the recrystallization, and are arguably coeval with the opening of voids in which the saddle dolomite (Dol 2) nucleated (Fig. 7A and B).

Uranium–lead (U-Pb) age data (164·0 to 194·1 Ma including errors) for Dol 1 and Dol 2 coincide with Early to Middle Jurassic tectonism that induced far-field hydrothermal pulses recorded across Europe (Walter *et al.*, 2018, and references therein). During several tectonic events, large portions of the upper crust were saturated with hot fluids through extensional basin-related fault systems, causing alteration of the basement and mineralization (Tritlla & Sole, 1999; Meyer *et al.*, 2000; Cathelineau *et al.*, 2012; Subias *et al.*, 2015; Munoz *et al.*, 2016). The dominant tectonic event was the rotation of Iberia, caused by the opening of the Proto-Atlantic (e.g. Wetzel *et al.*, 2003; Clauer *et al.*, 2008; Pfaff *et al.*, 2009; Brockamp *et al.*, 2011; Walter *et al.*, 2017). Most studies have primarily focused on the mineralization of clastic and magmatic Palaeozoic to Triassic rocks. Possibly for the first time, this large-scale hydrothermal event is now documented in carbonates. It seems likely that similar features are recorded across the Iberian region, but most studies lack constraining age data.

Despite many hydrothermal dolomite deposits (e.g. Davies & Smith, 2006; Jacquemyn *et al.*, 2014; Morrow, 2014) developing as replacement minerals of 'pure' LST precursors, the example documented here arguably evolved from a dolomite precursor, because only dolomite rhombs were preserved after the recrystallization of Dol 1.

Although the iron-rich Dol 3 is less common than Dol 1 and Dol 2, its partial corrosion (Fig. 6E and F) indicates a change in fluid chemistry and, likely, a precipitation hiatus. The subsequent Dol 4 and Dol 5 phases are characterized by fluid inclusion homogenization temperatures up to 250°C (medians of 215°C and 235°C, respectively; Fig. 8B, D and E) suggesting burial depths in excess of some thousands of metres (Davies & Smith, 2006; Hu *et al.*, 2018). Elevated fluid inclusion salinities (17 to 20 wt.% NaCl typical for basinal or continental basement brines; Frape *et al.*, 1984) distinguished Dol 4 and Dol 5 from paragenetically-older zebra saddle dolomite formed at shallower burial depths (Fig. 8F). A structural (morphological) roughness analysis (Renard *et al.*, 2004) of five bedding-parallel stylolites of the studied dolostone was calculated from the Fourier Power Spectra P(k) to estimate: (i) the compressive stress direction (Koehn *et al.*, 2012); (ii) the depth of formation (Bertotti *et al.*, 2017); and (iii) the amount of compaction (Ebner *et al.*, 2009b). Stylolite groups S1 and S2 (Figs 6C, 6D, 7A and 7B) formed under the same compaction-driven stress regime, at a calculated formation depth of 400 to 800 m and pressure of 10 to 18 MPa. These calculations do not imply high fluid temperatures related to deep burial. The S2 stylolites post-date Dol 5 (Fig. 6C and D) and, therefore, pre-date Alpine orogenesis, suggesting that bedding was still oriented horizontally when cement phases Dol 4 and Dol 5 formed.

Following Ingebritsen & Sanford (1998), rift-related geothermal convection is a possible mechanism to bring hot, deep-seated fluids into shallower burial environments. This is a likely explanation here, due to the short-lived pulses of hydrothermal fluids along extensional faults during the opening of the Proto-Atlantic in the Early Jurassic to Early Cretaceous. Braithwaite *et al.* (2004) discuss the common occurrence of deep seated thermobaric (Davies & Smith, 2006) fluid injection into the compactional regime. A significant implication of these data is that the dolostones remained within the same compaction-driven stress regime for nearly half of their diagenetic history (*ca* 100 Myr).

Hydrothermal and multistage tectonic overprint during the Alpine Orogeny

Following the precipitation of Dol 5, the contribution of hydrothermal fluids continuously decreased along the later diagenetic phases, becoming least significant in dolomite cement

phases 7 and 8 (215 to 250°C in Dol 5 versus 150 to 165°C in Dol 8; Fig. 8B, D and E). A high amount of fluid inclusions and the scattered occurrence of Dol 6 indicate significantly reduced precipitation rates (possibly a hiatus) with high fluid temperatures. Dol 7 and Dol 8 are characterized by similar fluid inclusion salinities relative to those of Dol 4 and Dol 5 (17 to 22 wt.% versus 17·5 to 20·5 wt.% NaCl, respectively; Fig. 8C and F). However, fluctuating fluid inclusion densities (1·02 to 1·10 g cm^{-3}; Fig. 8F) and lower homogenization temperatures (median of 155 to 165°C; Fig. 8B, D and E) help to differentiate Dol 7 and Dol 8 from Dol 4 and Dol 5 (Fig. 8B, D and E). The change in Dol 8 inclusions towards $CaCl_2$-fluid chemistries (Fig. 9) evidences dissolution of evaporites and hence a different fluid source. Moreover, Dol 7 heralds the onset of a different tectonic setting than the previous compactional regime. Thin section evidence indicates that Dol 7 and Dol 8 phases occlude pore space in tectonic dolostone breccia (Fig. 7C to F), which is attributed to early Alpine thrusting (Lonergan & Platt, 1995; Platt *et al.*, 2005).

Dolomite cements 7 and 8 yield comparable $\delta^{18}O$ values relative to the paragenetically-older phases, suggesting fluid-controlled homogenization (Fig. 13). Petrographic and geochemical data indicate that the homogenization event may be related to late-stage dolomite cementation. In contrast, Dol 7 and 8 are moderately ^{13}C-depleted ($\delta^{13}C_{min.} = -1{\cdot}7‰$, Table 1) relative to older precipitates. The patterns observed here are in good agreement with data from other structurally-controlled hydrothermal dolomites worldwide (Davies & Smith, 2006).

Arguments supporting Alpine orogenesis as the driver of large-scale fluid movement and formation of dolomite cements 7 and 8 include: (i) relative age constraints on the complex vein dolomite phases from cathodoluminescence analyses (Fig. 7); and (ii) the relation of these pore-filling fabrics in tectonic breccias of Alpine age that predate the Carboneras fault activity (as supported by previous regional studies). More specifically, contractional tectonism with Ar–Ar ages suggests Alpine Orogeny between the Eocene and Early Miocene (Monie *et al.*, 1991; Platt *et al.*, 2005). An initial phase of this major tectonic phase could likely be a trigger for the expulsion of hot, deep-seated saline continental basement brines (Fig. 9) that induced the precipitation of dolomite cements 7 and 8. Similar patterns have been reported in several earlier studies worldwide (i.e. Davies & Smith, 2006; López-Horgue *et al.*, 2010; Hendry *et al.*, 2015; Martín-Martín *et al.*, 2015; Dong *et al.*, 2017). A second, large-scale tectonic event is arguably recorded here, the modification of the European Cenozoic Rift System (Maillard & Mauffret, 1999; Walter *et al.*, 2018, and references therein) prior to, and during, the Alpine Orogeny. This stage may also have reactivated Jurassic to Cenozoic extensional faults, resulting in a proto-Carboneras fault system.

This progression of tectonic events was followed by accelerated burial in the Oligocene that caused high temperature and high pressure metamorphosis. During the Early Miocene, rapid exhumation of large areas of the Betic Cordilleras occurred (Vissers, 2012). Substantial evidence exists for greenschist facies metamorphism in bulk Alpujarride strata from analyses in metapelites, phyllites and calcareous/dolomitic 'marbles' (see e.g. Bakker *et al.*, 1989; Azañón & Crespo-Blanc, 2000; Vissers, 2012; and many others). Remarkably, late-stage, low-grade metamorphism with temperatures between 300°C and 430°C, did not transform the Carboneras dolostones into marble, as evidenced by the (albeit patchy) preservation of dolomite cements and their primary fluid inclusions (Figs 6 to 9).

Discrepancy between studies regarding burial depth of the dolostones analyzed here merits attention. According to Bakker *et al.* (1989) and Vissers (2012), the Alpujarride strata in the eastern Betics were buried to depths of 25 km (*P*: 700 MPa; *T*: 430°C) during the Eocene to Oligocene. These authors propose a reduced geothermal gradient of 17 to 20°C rather than 30°C per kilometre. Assuming that these assumptions are true, two possible interpretations exist: (i) Alpujarride dolostones were indeed buried to depths of 25 km and temperatures in excess of 400°C, but preserved their structural integrity, petrographic characteristics and even primary fluid inclusions; or (ii) the Alpujarride dolostones studied here experienced *P*/*T* pathways and burial histories that differed from other Alpujarride rock units. At present, neither of these interpretations are conclusive. Based on the presented evidence, it seems likely that deep burial over time spans of at least 20 to 25 Myr (Eocene to Oligocene) should have resulted in the neomorphosis of minerals typical of these conditions, such as periclase, brucite, phyllosilicates or serpentine (Ferry *et al.*, 2002; Bucher & Grapes, 2011), which are not found in the described units.

Moreover, even in an end-member type, rock-buffered system, carbonates are expected to recrystallize, albeit very slowly. This would occur in a diffusion-controlled system, and in the presence of thin fluid films at crystal boundaries or along reaction fronts (Pingitore, 1982; Watson & Müller, 2009; Jonas *et al.*, 2017; Pederson *et al.*, 2019). These slow, fabric-preserving micro-scale dissolution–recrystallization processes are probably under-appreciated and under-explored from a carbonate archive perspective. Clearly, Alpujarride dolostones experienced physical and chemical compaction during burial, and Dol 2 to Dol 5 cements occluded the remaining pore space, resulting in fabric that was generally impermeable for fluids. However, even at great depths, spatially-localized (overpressured) pathways for aqueous fluids exist along fractures and fault systems, often resulting in complex diagenetic systems. Considering the data discussed here, it seems likely that these dolostones experienced peak burial depths of *ca* 15 km and temperatures of up to 300°C. Deeply-buried, low porosity dolostones – not yet transformed to marbles – have been reported from other low-grade metamorphic zones in the Alpine orogen. For example, low porosity, Upper Triassic to Lower Jurassic dolostones in the Alpi Apuane (north-west Italy), preserved their textures under temperatures up to 300°C, and only then did recrystallization commence (Cortecci *et al.*, 1999; Molli *et al.*, 2018, and references therein).

In summary, the dolostones comprising the uppermost units of the Alpujarride preserved most of their early diagenetic textures even under low-grade metamorphic conditions or, alternatively, underwent fabric-preserving micro-scale recrystallization. However, the observation of primary fluid-inclusions in these rocks does not support the latter scenario. Timing of the homogenization of dolomite $\delta^{18}O$ signatures of all cement phases pre-dating (and potentially including) Dol 7 and Dol 8 remains speculative. Considering the previously mentioned rock-buffered and fluid-lean system, extended durations (Early Eocene to Early Miocene) and temperatures *ca* 300°C would be required for the slow diffusion processes to occur across thin fluid films at crystal boundaries to facilitate $\delta^{18}O$ homogenization. These processes are poorly understood from a mechanistic and kinetic perspective, and further well-calibrated experimental work is needed.

Tectonic and renewed hydrothermal overprint in the Carboneras Fault Zone

Evidence for the overprint of fault zone rocks comes (among other aspects) from the relationship between allochthonous dolostones and autochthonous transgressive deposits of the Carboneras Nijar Basin. The Azagador Formation with marine invertebrate remains (Fig. 3) evidences the flooding of the fault zone during the Late Tortonian. Although no direct evidence exists for the timing of subsequent events that led to varying degrees of cataclasation in the fault zone (Fig. 14), the position of dolostone blocks in the Fault Zone and the described paragenetic sequence suggest that this process occurred during the main phase of tectonic activity (Middle to Late Serravallian).

Based on dolomite geochemistry, an increasing degree of brecciation and cataclasation (Figs 11 and 13) coincides with a $\Delta^{18}O$ of 4‰ between early marine dolomicrite Dol 1 and cataclasite C 1 (Fig. 13). Importantly, not only the cataclastic matrix yields ^{18}O-enriched values compared to the 'precursor' phases, but a resetting of the Dol 1 clasts within this breccia is also observed. This indicates an exchange between fault zone fluids and rock fragments, potentially due to a newly increased permeability. The fluid-dominated fault system and the large surface area to volume ratio of clasts facilitated the resetting of bulk $\delta^{18}O$ signatures. The shift to higher $\delta^{18}O$ values – approaching seawater composition – in a hydrothermal fault zone merits discussion.

The Late Tortonian marine flooding of the fault zone best explains this counterintuitive isotopic shift. Seawater percolated downward into the fault zone where it was heated, and later re-ascended. The volume of seawater relative to hydrothermal fluids in the shallow domain of a submerged fault zone is high enough that a shift towards seawater chemistry is reasonable (Fig. 15). Comparing reconstructed $\delta^{13}C_{DIC}$ values of Late Triassic seawater (brachiopod shells; Saltzman & Thomas, 2012) to Middle Miocene to Recent oceans, an obvious overlap is observed (Fig. 13). The implication of this is a convoluted differentiation between 'typical' Late Triassic and 'typical' Middle Miocene seawater values. Furthermore, $\delta^{13}C$ values compiled here plot within the range of either of these potential source waters. Consideration regarding mineralogy-dependent (calcite versus dolomite) fractionation are moot, because the

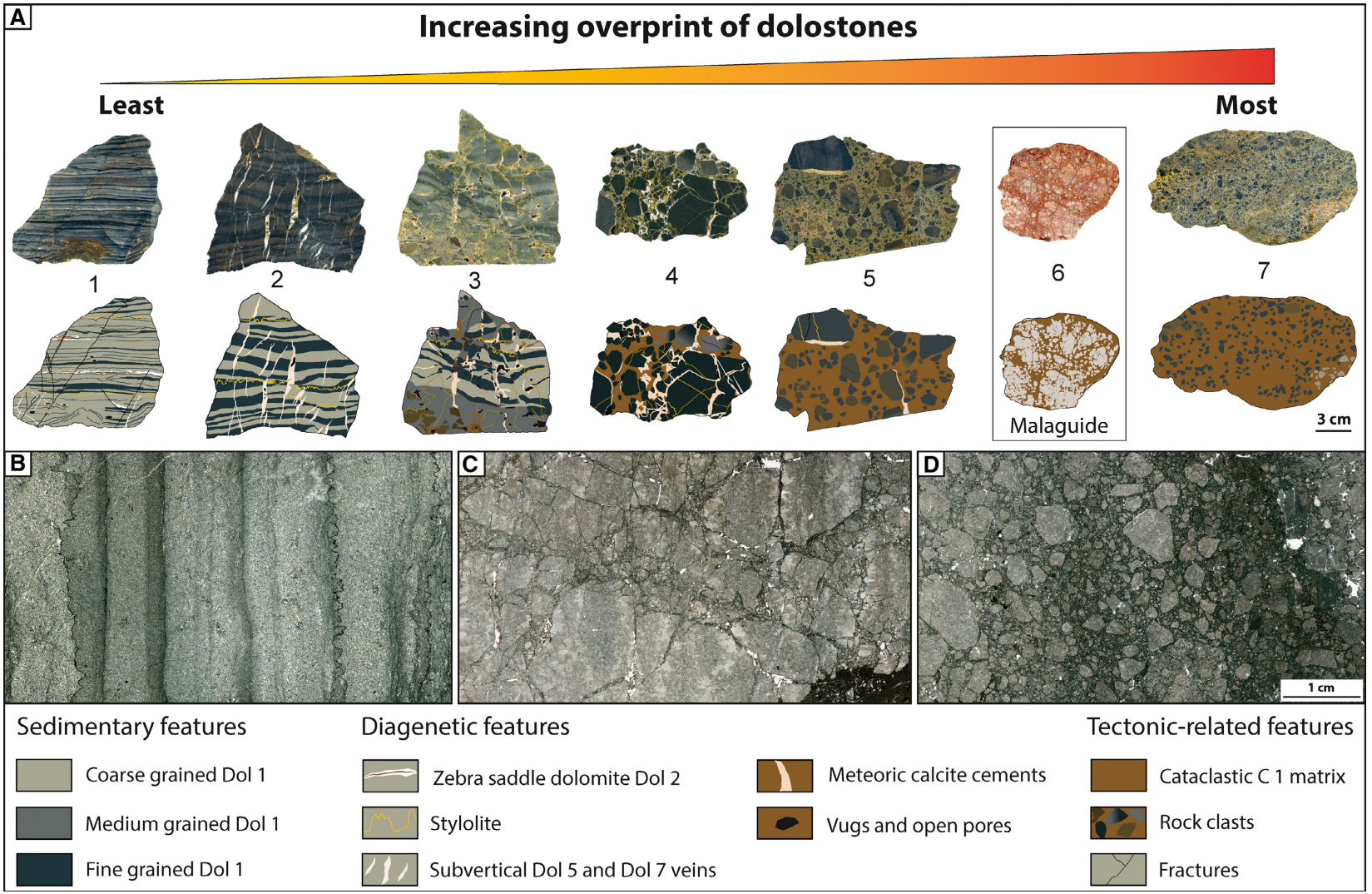

Fig. 14. (A) Sequence (1 = least; 7 = most) of diagenetic and tectonic overprint. Sedimentary-related, diagenetic-related and tectonic-related features are indicated at the bottom. Note that sequence stage 6 represents a sample that was geochemically characterized as Malaguide dolostone. (B) Transmitted light image of Early diagenetic dolostone Dol 1. The host rock is strongly recrystallized but contains grain-size related fine lamination and S1 stylolites. (B) Brecciated early diagenetic dolostone Dol 1 with some zebra saddle Dol 2 and little cataclastic C 1 content. (C) Cataclastic C 1 with early diagenetic dolostone Dol 1 clasts of different grain size from different areas of the dolomitized carbonate platform.

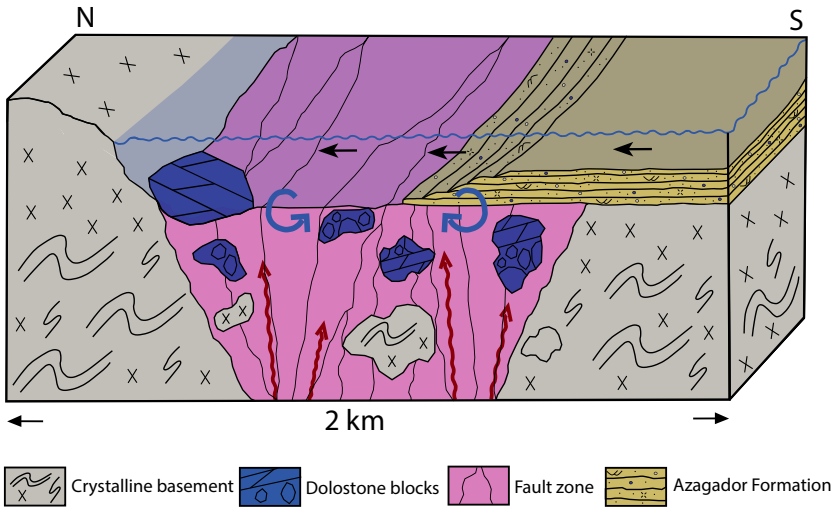

Fig. 15. Conceptual sketch for dolostone position and fluid sources during Neogene overprint of Alpujarride dolostones. Seawater entered the Carboneras Fault Zone during the early stages of formation of the Carboneras Nijar Basin to the south. The dolostones were in a shallow burial position, hence seawater enriched in radiogenic strontium from the continental crust and nearby volcanic complexes was the dominant diagenetic fluid. Despite these potential sources of alteration, none is clearly visible in geochemical data.

enrichment of ^{13}C in dolomite relative to calcite (*ca* 1‰; Swart, 2015) is only significant in fluids at Earth surface conditions, and is insignificant at elevated fluid temperatures such as in burial environments. In principle, two end-member interpretations exist. The first being that dolomites preserved a primarily Late Triassic seawater $\delta^{13}C_{DIC}$ signature that was not significantly altered during subsequent burial and overprint in the fault zone. This interpretation assumes a rock-controlled diagenetic environment with regard to $\delta^{13}C$. The absence of ^{13}C-enrichment from the degassing of magmatic CO_2 from intrusions into the fault zone provides circumstantial evidence of this. Carbon isotope fractionation during the uptake of magmatically-derived CO_2 from HCO_{3-} in marine waters (Chacko *et al.*, 2001, and references therein) yields approximately +3‰, which is believed to sufficiently enrich the local marine $\delta^{13}C$ signature (Jacquemyn *et al.*, 2014)

Alternatively, Fig. 13 illustrates that all dolomite $\delta^{13}C$ values plot in the lower portions (*ca* 0 to +2‰) of the reconstructed Triassic seawater values that overlap with the range of Miocene to Recent seawater $\delta^{13}C_{DIC}$. This interpretation suggests a pervasive re-equilibration of all dolomite phases with respect to carbon isotopes, and a shift towards Miocene seawater $\delta^{13}C_{DIC}$. This controversy cannot presently be resolved by means of carbon isotope data alone, and additional lines of evidence must be considered, including $^{87}Sr/^{86}Sr$ ratios (Fig. 16) and petrography. The observation of well-preserved zoning of Dol 3 to Dol 8 cements (Fig. 6E and H) contrasts the theory of pervasive carbon isotope re-equilibration with Miocene seawater. Although some of these zones are internally patchy (Fig. 6F and H), zoning at a scale of some tens of micrometres is well-preserved. Given that pervasive re-equilibration of dolomite $\delta^{13}C$ values is only possible via a micro-scale dissolution–reprecipitation mechanism, and would be expected to obliterate the subtle chemical zonation, the possibility of this mechanism can be excluded.

All studied dolomite phases plot outside of reconstructed Middle/Late Triassic seawater $^{87}Sr/^{86}Sr$ ratios and shift towards the possibly more radiogenic Miocene ratios (Fig. 16). As expected, the cataclastic matrix represents an endmember stage of dolomite alteration and hydrothermal overprint, with $^{87}Sr/^{86}Sr_{C1}$ ratios in reasonable agreement with Miocene data, or are even more radiogenic. The latter observation is best explained by the highly radiogenic values of crust-derived fluids that interacted with Rb-bearing minerals, typical for deep-reaching fault zones (Fig. 16; Faure *et al.*, 1963; Perry & Turekian, 1974; Dong *et al.*, 2017). However, hydrothermal fluids from magmatic bodies in (or near) the Carboneras Fault Zone must also be considered (Benito *et al.*, 1999; Mattei *et al.*,

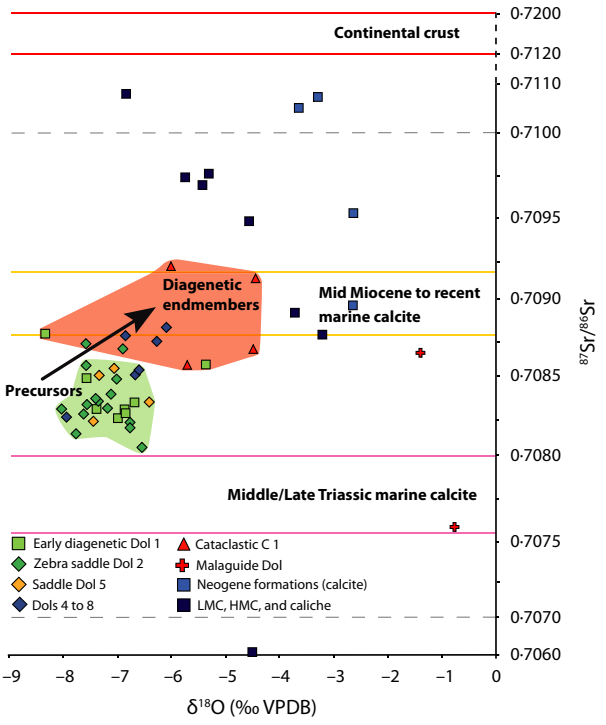

Fig. 16. Oxygen isotopic composition plotted against strontium isotopic composition of dolomite and calcite phases compared to Middle Miocene to Recent and Middle/Late Triassic unaltered marine calcites and continental crust (from Korte *et al.*, 2003; Banner, 2004; McArthur *et al.*, 2012). The annotated trend indicates a $\delta^{18}O$ and $^{87}Sr/^{86}Sr$ shift towards a recent marine calcite strontium isotope composition from dolomitic precursor phases towards dolomitic cataclasite. VPDB, Vienna-Pee Dee Formation belemnite.

2014) as sources for highly-radiogenic strontium. In contrast to the cataclasite values, the early diagenetic dolomicrite phases (Dol 1 and Dol 2) plot near Triassic seawater values. However, even small amounts of material with a highly radiogenic signature of crust-derived fluids would affect bulk samples to a disproportional degree, such as the case for Dol 1. This is exemplified in values of autochthonous Neogene calcitic units that plot significantly outside of the range of Miocene seawater (Fig. 16).

Assessing all available data, a significant re-equilibration of Triassic $^{87}Sr/^{86}Sr_{dolomite}$ ratios and carbon isotope values in the presence of Miocene (or younger) seawater or crust-derived hydrothermal fluids (Fig. 15) seems unlikely, due to: (i) lack of evidence for a ^{13}C-enriched CO_2 source for $\delta^{13}C_{dolomite}$; (ii) a moderate shift of bulk dolostones towards more radiogenic $^{87}Sr/^{86}Sr$ ratios; (iii) the contamination bias of Dol 1 samples with material yielding radiogenic Sr; and (iv) a well-preserved (albeit patchy) zonation (Fig. 6F and H) of dolomite cements, ruling out bulk dissolution–reprecipitation.

Marine transgressive deposits and late stage meteoric diagenesis

The isotope geochemistry of marine bivalve shells sampled in the autochthonous Azagador Formation that transgressed the fault zone displays typical Miocene marine calcite values. In contrast, bulk sediment samples are significantly more negative in both their oxygen and carbon composition. Connate fluids present during deposition of these and other Neogene strata from the Carboneras Nijar Basin had no observable impact on impermeable Alpujarride dolostones. The latest paragenetic stage, characterized by a regression and subaerial exposure of the sea floor, is identified by authigenic quartz (Qz 1), and blocky low-Mg and high-Mg calcite meteoric cements (LMC 1 to LMC 4 and HMC 1 to HMC 3; Fig. 11). In the field area, dolostones are typically covered by a decimetre-thick calcitic caliche soil, i.e. a subrecent weathering product of carbonates typical for a semi-arid climate (James & Choquette, 1990). Carbon isotope values of late meteoric–vadose calcite cements, speleothems and caliche are between $-10‰$ and $-5‰$. Studies have proven a significant impact on $\delta^{13}C$ compositions (-10 to $2‰$) of Caribbean Pleistocene LSTs driven by ^{12}C contribution associated with the decay of organic material (Lohmann, 1987; James & Choquette, 1990). Values for the aforementioned meteoric–vadose samples reported here (calcite cements, speleothems and caliche) agree with these findings. However, a significant overprint of paragenetically older dolomite cement phases was not found. This may be related to low fluid circulation within the low porosity and permeability dolostone, and high resistance of these phases to changes in their $\delta^{13}C$ composition at near-surface conditions. In summary, the geologically-younger regressive intervals and the subsequent meteoric stages did not significantly affect the dolostones of interest here.

The multi-proxy approach conducted here includes radiometric age dating of specific cement phases and allows for a detailed reconstruction of a complex history of dolomitization and tectonic/hydrothermal overprint. Refer to Fig. 17 for an overview of all depositional, diagenetic and tectonic stages including the reconstructed burial history of the Alpujarride dolostones.

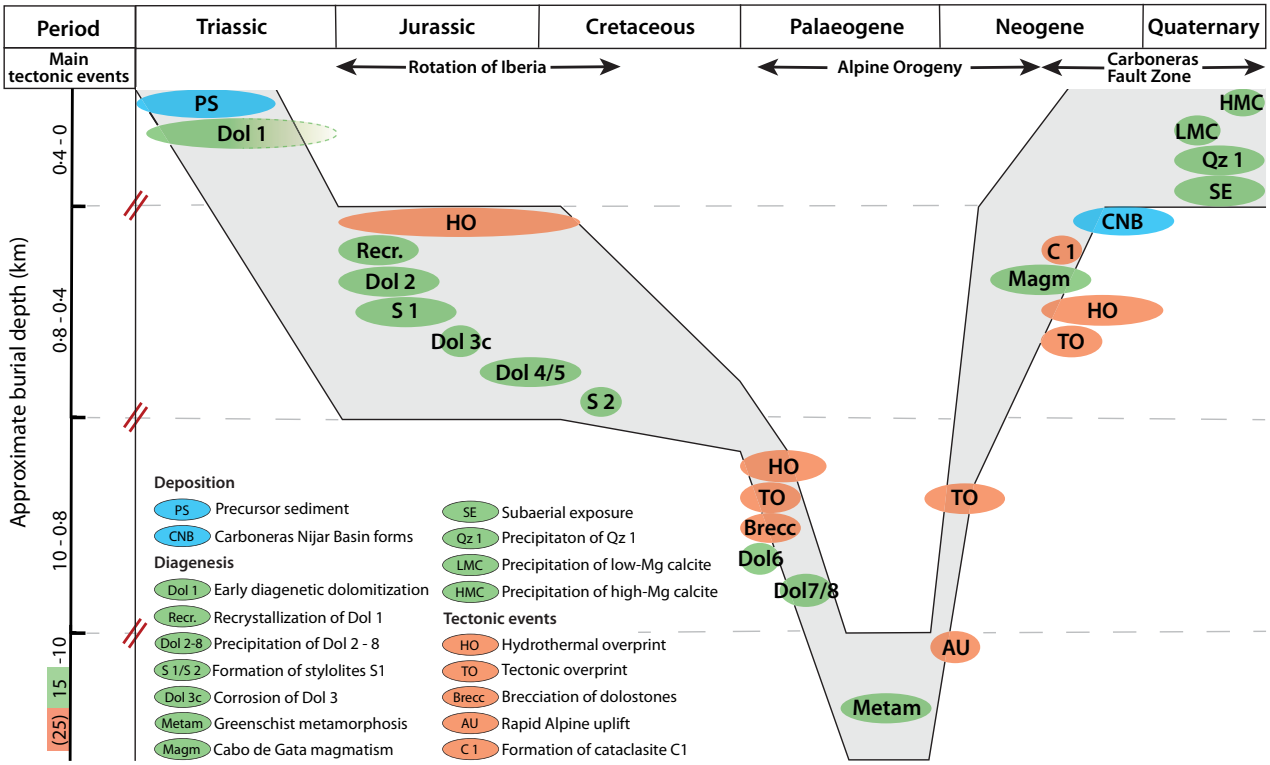

Fig. 17. Interpreted burial history, tectonic events and the associated diagenetic processes affecting Alpujarride dolostones from deposition in the Middle/Late Triassic to Recent. Large-scale tectonism includes the rotation of Iberia, Alpine Orogeny and Carboneras Fault Zone activity. Interpreted maximum burial depth of *ca* 10 to 15 km for Alpujarride dolostones is given in green, whereas bulk Alpujarride rocks (25 km) after Bakker *et al.* (1989) and Vissers (2012) are shown in orange. Associated depths during precipitation correspond to pressure correction of fluid inclusion analysis. Burial depth not at uniform scale.

Malaguide dolostones and their diagenetic pathways

In contrast to Alpujarride dolostones comprising the focus of this study, Malaguide dolostones rarely occur in the study area. These deposits have carbon and oxygen compositions similar to Middle/Late Triassic and Middle Miocene to Recent marine calcite. The precursor facies of the Malaguide dolostones was deposited, in part contemporaneously, a few 100 km south of the Alpujarride platform system (Sanz de Galdeano *et al.*, 2001). Malaguide $\delta^{18}O$ values suggest diagenetic pathways differing from those of Alpujarride dolostones. The nearly 3·5‰ gap between the isotopically heaviest Alpujarride (C 1 matrix) dolomite relative to Malaguide dolomites can arguably be explained by: (i) a comparably simple paragenetic succession in Malaguide carbonates relative to the more complex Alpujarride dolomites; and (ii) transport under compressional Alpine tectonism over hundreds of kilometres to their present day position, combined with a comparably shallow burial depth of Malaguide units. Note that the latter rock units form part of the uppermost tectonic slice in the Betic Cordilleras (Lonergan & Platt, 1995; Vissers, 2012; Rutter *et al.*, 2012, and references therein). Johnson (1993) proposed peak temperatures of 200°C based on fission track analysis, whereas Lonergan & Platt (1995) proposed that the stratigraphically lowermost Malaguide dolostones reached low-grade anchizone conditions. Contrastingly, Critelli *et al.* (2008) analyzed red beds interstratified with Malaguide dolostones and proposed burial temperatures of 100 to 160°C and lithostatic/tectonic loading of 4 km. Independent of these varying interpretations, the differences in burial depth and temperatures between Alpujarride and Malaguide strata resulted in two different diagenetic pathways, as supported by the contrasting data found here (Bakker *et al.*, 1989; Vissers, 2012). It is plausible that a detailed comparison of these two dolostone units could have its merits, but a different study area that offers equal access to both units must be chosen.

Implications for ancient dolostone archives

In the following, data shown here are critically set in context with previously published work utilizing marine or early diagenetic dolostones as palaeoenvironmental archives. The number of papers dealing with dolomite as palaeoenvironmental archives for the Phanerozoic is comparably limited (e.g. Richter *et al.*, 2014; Geske *et al.*, 2015b; Hood *et al.*, 2018, and references therein), and is clearly related to the relative scarcity of Phanerozoic early diagenetic dolomite compared to the abundant biogenic material and bulk carbonate micrite (Turpin *et al.*, 2014, and references therein). In the absence of biogenic carbonates in the deep time rock record, dolomite archives become disproportionally more important (Tucker, 1982; Burns & Matter, 1993; Halverson *et al.*, 2005; Mazumdar & Strauss, 2006; Kasemann *et al.*, 2014; Cui *et al.*, 2017; and references therein). Complications arise from the fact that Precambrian dolomite archives are either direct marine precipitates (Tucker, 1983; Hood *et al.*, 2011; Wood *et al.*, 2017; Shuster *et al.*, 2018), early to late diagenetic replacement phases of aragonitic, calcitic or dolomitic precursors, or direct pore-filling precipitates of deep-seated hydrothermal fluids. Work shown here and in previous studies, represents a clear note of caution that the uncritical use of geochemical data from bulk dolostones, possibly mixed with that from LSTs, must be avoided (e.g. Magaritz *et al.*, 1986; Lambert *et al.*, 1987; Jenkins *et al.*, 1992; Shen *et al.*, 1998; Melezhik *et al.*, 2009). More recently, the number of studies critically balancing environmental and diagenetic patterns is increasing (e.g. Kaufman & Knoll, 1995; Knauth & Kennedy, 2009; Derry, 2010a; Grotzinger *et al.*, 2011). Well-constrained studies disentangling Neoproterozoic cement parageneses include Cui *et al.* (2016c, 2017), Zhou *et al.* (2016) or Hood *et al.* (2018). Moreover, non-conventional proxies, such as boron isotopes and calcium isotopes (Kasemann *et al.*, 2005), magnesium isotopes (Kasemann *et al.*, 2014), clumped isotope palaeothermometry (Loyd *et al.*, 2015) and cadmium isotopes (Hohl *et al.*, 2017), may offer a new perspective of the Neoproterozoic world. Using the Carboneras Fault Zone dolostones to test the resistance of these proxies to complex diagenetic overprint may be worthwhile.

Regarding the Neoproterozoic rock record, many dolomitization models, as based on Phanerozoic case studies, must be considered with caution due to some fundamentally different environmental parameters (Algeo *et al.*, 2015; Canfield *et al.*, 2008). An issue with the interpretation of Ediacarian rocks is the uncertainty of seawater $\delta^{18}O$ values. Many models exist, but none are based on empirical evidence, or able to answer all associated questions (see Cui *et al.*, 2017, and references therein). Taking the results of this study and previous work into account, it is clear that $\delta^{18}O$ dolomite signatures are generally prone to diagenesis, and may even react to retrograde alteration. In the case example shown here, a $\Delta^{18}O$ of 4‰ between the early marine dolomicrite Dol 1 and cataclasite C 1 is observed. The authors acknowledge that most would not consider Proterozoic cataclasite as archives of marine isotope values, but the general warning is clear, that even in diagenetically-stable carbonate phases such as stoichiometric dolomite, $\delta^{18}O$ values are potentially compromised. In contrast, dolomite $\delta^{13}C$ signatures in rock-buffered, fluid-lean systems are remarkably well-preserved even under extreme conditions.

Despite all of these issues, it is encouraging that early diagenetic (fabric-preserving) replacement dolomites precipitated from (near) marine porewaters, are possible archives for marine climate dynamics of the ancient Earth, independent of the chosen time interval. Problems that may result when exploiting early diagenetic dolomites lie in their often non-stoichiometric, Ca-rich nature (Geske *et al.*, 2015b) and from any complex amorphous precursors (Mavromatis *et al.*, 2017). When the subsequent stabilization to a stoichiometric $Mg/CaCO_3$ occurs in the presence of marine shallow burial fluids, a diagenetically-stable archive is formed. This study provides evidence for this concept and encourages the use of a broad suite of analytical proxies. For example, and as suggested by Derry (2010a), fluid inclusion studies of Neoproterozoic rocks are still surprisingly scarce. Data reported here, and in many previous studies, demonstrate that fluid inclusion analysis is a powerful tool to examine primary fluid inclusion temperature ranges from 50 to 250°C, even in dolostones that have experienced low-grade overprint at temperatures up to 300°C.

CONCLUSIONS

The multi-proxy study discussed here documents a test of preservation potential of marine

dolomite archive proxy data to extreme, long-term diagenesis, including low-grade metamorphosis. As the product of these events, eight dolomite phases, a dolomitic cataclasite and a series of meteoric/vadose calcite cements resulted, and are here characterized in terms of petrographic, paragenetic and geochemical criteria.

The complex geological history of these dolostones commenced in the Middle to Late Triassic with protolith deposition and fabric-preserving, early marine to shallow marine burial replacive dolomitization (Dol 1) at maximum fluid temperatures of 50°C. During intermediate burial, zebra saddle dolomite formed while the bulk rock further recrystallized at temperatures up to 150°C (Dol 2). Phase Dol 1 recrystallization and Dol 2 formation likely occurred during an interval of large-scale tectonism related to the rotation of Iberia and the opening of the Proto-Atlantic Ocean during the Early–Middle Jurassic, when deep hydrothermal fluids ascended to shallower levels. Corrosion of Dol 3 cement marks a change to undersaturation in the fluids with respect to dolomite. Phases Dol 4 and Dol 5 are likely also related to the rotation of Iberia, and have peak fluid inclusion homogenization temperatures of 250°C. Dolomite phases 1 to 5 were precipitated in a compactional regime that did not significantly change over *ca* 100 Myr. Phase Dol 6 represents a relatively quiescent duration in terms of precipitation, as a consequence of low remaining porosity due to physical and chemical compaction. The subsequent Dol 7 and Dol 8 cement phases signify a fundamental change to a deeper tectonic setting during an early phase of the Alpine Orogeny. High-grade anchizone conditions did not cause dolostones to evolve into marble fabrics, and these rocks have striking textural preservation as documented by their primary fluid inclusions. Timing of deep, hot, dolomite cement precipitation and subsequent homogenization of $\delta^{13}C$ and $\delta^{18}O$ occurred during the Early Eocene to Early Miocene. During the main phase of the fault zone activity (Middle to Late Serravallian), the dolostones experienced an increasing degree of brecciation and cataclasation, coupled with a significant fluid-dominated shift in dolomite $\delta^{18}O$ values. Despite these multi-stage tectono-hydrothermal events, early marine diagenetic replacive dolomites preserved their Late Triassic seawater dissolved inorganic carbon (DIC) and $^{87}Sr/^{86}Sr$ signatures. This is considered to be evidence for an uncommonly conservative nature of some, but not all, of these geochemical proxies.

The term 'dolomite' should be used with caution, because it is sometimes used in a simplified manner for an often complex suite of early marine to late burial Mg-carbonates, each of which represent different physico-chemical parameters and proxy data. Therefore, the interpretation of dolostone data without a robust petrographic framework is discouraged. One should also acknowledge that isotope or elemental proxy data will likely vary in their recalibration or stabilization based on a fluid-buffered or rock-buffered system. This implies that the same dolomite archive may yield well-preserved or highly-altered data depending on the analyzed proxy and diagenetic environment. Evidence is given that petrographic criteria for alteration does not necessarily imply either a resetting or preservation of the proxy data.

ACKNOWLEDGEMENTS

This study was performed in the context of the collaborative research initiative CHARON Phase II (DFG Forschergruppe 1644). The authors thank B. Gehnen and K. Krimmler from the isotope geochemistry laboratory for isotope analysis, S. Weisel, M. Born, A. Schulz and T. Seemann from the thin section preparation department, T. Reinecke and H. Mammen for X-ray diffraction analysis, and N. Jöns for microprobe analysis at Ruhr-University Bochum. Additional thanks go to R. Coimbra from the University of Aveiro for help with regional geological literature and to R. Stritzke from the Geological Survey of North Rhine-Westphalia for spores and pollen analysis in dolostones. Special thanks go to R. Hoffmann, A. Hueter, L. Wulff and Y. Hu for their time and helpful comments which helped to improve this paper, and to J. Parr for assistance in sample preparation and drawing of figures. The authors express their gratitude to the journal editors Dr G. Della Porta and Dr H. Qing, as well as to reviewers Dr D. Morrow and an anonymous colleague. Special thanks go to Dr Morrow for his extremely thorough review. Sampling of rocks was not possible in the Cabo de Gata Natural Parc due to legal restrictions. However, the Carboneras Fault Zone expands beyond the boundaries of the Natural Park, where sampling of all relevant lithologies is possible. The authors also made use of extensive rock collections at the Ruhr-University Bochum that stem from several unpublished

PhD projects performed in the 1970s and 1980s in this region.

REFERENCES

Algeo, T.J., **Luo, G.M.**, **Song, H.Y.**, **Lyons, T.W.** and **Canfield, D.E.** (2015) Reconstruction of secular variation in seawater sulfate concentrations. *Biogeosciences*, **12**, 2131–2151.

Alonso-Chaves, F.M., **Soto, J.I.**, **Orozco, M.**, **Kilias, A.A.** and **Tranos, M.D.** (2004) Tectonic evolution of the betic cordillera: an overview. *Bull. Geol. Soc. Greece*, **XXXVI**, 1598–1607.

Arvidson, R.S., **Mackenzie, F.T.** and **Guidry, M.** (2006) MAGic: a Phanerozoic model for the geochemical cycling of major rock-forming components. *Am. J. Sci.*, **306**, 135–190.

Arvidson, R.S., **Guidry, M.W.** and **Mackenzie, F.T.** (2011) Dolomite controls on phanerozoic seawater chemistry. *Aquat. Geochem.*, **17**, 735–747.

Azañón, J.-M. and **Crespo-Blanc, A.** (2000) Exhumation during a continental collision inferred from the tectonometamorphic evolution of the Alpujarride Complex in the central Betics (Alboran Domain, SE Spain). *Tectonics*, **19**, 549–565.

Bakker, R.J. and **Diamond, L.W.** (2006) Estimation of volume fractions of liquid and vapor phases in fluid inclusions, and definition of inclusion shapes. *Am. Miner.*, **91**, 635–657.

Bakker, H.E., **Jong, K.D.**, **Helmers, H.** and **Biermann, C.** (1989) The geodynamic evolution of the Internal Zone of the Betic Cordilleras (south-east Spain): a model based on structural analysis and geothermobarometry. *J. Metamorph. Geol.*, **7**, 359–381.

Banner, J.L. (2004) Radiogenic isotopes: systematics and applications to earth surface processes and chemical stratigraphy. *Earth Sci. Rev.*, **65**, 141–194.

Benito, R., **López-Ruiz, J.**, **Cebriá, J.M.**, **Hertogen, J.**, **Doblas, M.**, **Oyarzun, R.** and **Demaiffe, D.** (1999) Sr and O isotope constraints on source and crustal contamination in the high-K calc-alkaline and shoshonitic neogene volcanic rocks of SE Spain. *Lithos*, **46**, 773–802.

Bertotti, G., **de Graaf, S.**, **Bisdom, K.**, **Oskam, B.**, **Vonhof, H.B.**, **Bezerra, F.H.R.**, **Reijmer, J.J.G.** and **Cazarin, C.L.** (2017) Fracturing and fluid-flow during post-rift subsidence in carbonates of the Jandaíra Formation, Potiguar Basin, NE Brazil. *Basin Res.*, **29**, 836–853.

Birck, J.L. (1986) Precision K-Rb-Sr isotopic analysis: application to Rb-Sr chronology. *Chemical Geology*, **56**, 73–83.

Bontognali, T.R.R., **Vasconcelos, C.**, **Warthmann, R.J.**, **Bernasconi, S.M.**, **Dupraz, C.**, **Strohmenger, C.J.** and **Mckenzie, J.A.** (2010) Dolomite formation within microbial mats in the Coastal Sabkha of Abu Dhabi (United Arab Emirates). *Sedimentology*, **57**, 824–844.

Braithwaite, C.J., **Rizzi, G.** and **Darke, G.** (2004) *The Geometry and Petrogenesis of Dolomite Hydrocarbon Reservoirs*. Geological Society of London, London, UK.

Brockamp, O., **Schlegel, A.** and **Clauer, N.** (2011) Mesozoic hydrothermal impact on Rotliegende and Bunter immature sandstones of the High Rhine trough and its adjacent eastern area (southern Black Forest, Germany). *Sed. Geol.*, **234**, 76–88.

Bucher, K. and **Grapes, R.** (2011) Metamorphism of dolomites and limestones. In: *Petrogenesis of Metamorphic Rocks*, pp. 225–256. Springer, Berlin, Heidelberg.

Burns, S.J. and **Matter, A.** (1993) Carbon isotopic record of the latest proterozoic from Oman. *Eclogae Geol. Helv.*, **86**, 595–607.

Canfield, D.E., **Poulton, S.W.**, **Knoll, A.H.**, **Narbonne, G.M.**, **Ross, G.**, **Goldberg, T.** and **Strauss, H.** (2008) Ferruginous conditions dominated later neoproterozoic deep-water chemistry. *Science*, **321**, 949–952.

Cathelineau, M., **Boiron, M.-C.**, **Fourcade, S.**, **Ruffet, G.**, **Clauer, N.**, **Belcourt, O.**, **Coulibaly, Y.**, **Banks, D.A.** and **Guillocheau, F.** (2012) A major Late Jurassic fluid event at the basin/basement unconformity in western France: $^{40}Ar/^{39}Ar$ and K–Ar dating, fluid chemistry, and related geodynamic context. *Chem. Geol.*, **322–323**, 99–120.

Chacko, T., **Cole, D.R.** and **Horita, J.** (2001) Equilibrium oxygen, hydrogen and carbon isotope fractionation factors applicable to geologic systems. *Rev. Mineral. Geochem.*, **43**, 1–81.

Clauer, N., **Liewig, N.**, **Ledesert, B.** and **Zwingmann, H.** (2008) Thermal history of Triassic sandstones from the Vosges Mountains-Rhine Graben rifting area, NE France, based on K-Ar illite dating. *Clay Miner.*, **43**, 363–379.

Cortecci, G., **Dinelli, E.**, **Indrizzi, M.C.**, **Susini, C.** and **Adorni Braccesi, A.** (1999) The apuane alps metamorphic complex, Northern Tuscany: chemical and isotopic features of grezzioni and marmi dolomitici. *Atti Soc. Tosc. Sci. Nat., Mem. Serie A*, **106**, 79–89.

Critelli, S., **Mongelli, G.**, **Perri, F.**, **Martín-Algarra, A.**, **Martín-Martín, M.**, **Perrone, V.**, **Dominici, R.**, **Sonnino, M.** and **Najib Zaghloul, M.** (2008) Compositional and geochemical signatures for the sedimentary evolution of the Middle Triassic-Lower Jurassic continental redbeds from Western-Central Mediterranean Alpine Chains. *J. Geol.*, **116**, 375–386.

Cui, H., **Xiao, S.**, **Zhou, C.**, **Peng, Y.**, **Kaufman, A.J.** and **Plummer, R.E.** (2016c) Phosphogenesis associated with the Shuram Excursion: petrographic and geochemical observations from the Ediacaran Doushantuo Formation of South China. *Sed. Geol.*, **341**, 134–146.

Cui, H., **Kaufman, A.J.**, **Xiao, S.**, **Zhou, C.** and **Liu, X.-M.** (2017) Was the Ediacaran Shuram Excursion a globally synchronized early diagenetic event? Insights from methane-derived authigenic carbonates in the uppermost Doushantuo Formation, South China. *Chem. Geol.*, **450**, 59–80.

Davies, G.R. and **Smith, L.B.** (2006) Structurally controlled hydrothermal dolomite reservoir facies: an overview. *Am. Asso. Petrol. Geol. Bull.*, **90**, 1641–1690.

Delgado, F., **Estévez, A.**, **Martín, J.M.** and **Martín-Algarra, A.** (1981) Observaciones sobre la estratigrafía de la formación carbonatada de los mantos alpujárrides (Cordillera Bética). *Estud. Geol.*, **37**, 45–57.

Derry, L.A. (2010a) A burial diagenesis origin for the Ediacaran Shuram-Wonoka carbon isotope anomaly. *Earth Planet. Sci. Lett.*, **294**, 152–162.

Derry, L.A. (2010b) On the significance of $\delta^{13}C$ correlations in ancient sediments. *Earth Planet. Sci. Lett.*, **296**, 497–501.

Dong, S., **Chen, D.**, **Zhou, X.**, **Qian, Y.**, **Tian, M.** and **Qing, H.** (2017) Tectonically driven dolomitization of Cambrian to Lower Ordovician carbonates of the Quruqtagh area, north-eastern flank of Tarim Basin, north-west China. *Sedimentology*, **64**, 1079–1106.

Ebner, M., **Koehn, D.**, **Toussaint, R.**, **Renard, F.** and **Schmittbuhl, J.** (2009b) Stress sensitivity of stylolite morphology. *Earth Planet. Sci. Lett.*, **277**, 394–398.

Farkaš, J., **Böhm, F.**, **Wallmann, K.**, **Blenkinsop, J.**, **Eisenhauer, A.**, **van Geldern, R.**, **Munnecke, A.**, **Voigt, S.**

and **Veizer, J.** (2007) Calcium isotope record of Phanerozoic oceans: Implications for chemical evolution of seawater and its causative mechanisms. *Geochim. Cosmochim. Acta*, **71**, 5117–5134.

Faulkner, D.R., **Lewis, A.C.** and **Rutter, E.H.** (2003) On the internal structure and mechanics of large strike-slip fault zones: field observations of the Carboneras fault in southeastern Spain. *Tectonophysics*, **367**, 235–251.

Faulkner, D.R., **Mitchell, T.M.**, **Rutter, E.H.** and **Cembrano, J.** (2008) On the structure and mechanical properties of large strike-slip faults. *Geol. Soc. Spec. Publ.*, **299**, 139–150.

Faure, G. and **Powell, J.L.** (1972) *Strontium Isotope Geology*, 1st edn. Springer, Berlin, Heidelberg.

Faure, G., **Hurley, P.M.** and **Fairbairn, H.W.** (1963) An estimate of the isotopic composition of strontium in rocks of Precambrian Shield of North America. *J. Geophys. Res.*, **68**, 2323–2329.

Ferry, J.M., **Wing, B.A.**, **Penniston-Dorland, S.C.** and **Rumble, D.** (2002) The direction of fluid flow during contact metamorphism of siliceous carbonate rocks: new data for the Monzoni and Predazzo aureoles, northern Italy, and a global review. *Contrib. Mineral. Petrol.*, **142**, 679–699.

Fortuin, A.R. and **Krijgsman, W.** (2003) The Messinian of the Nijar Basin (SE Spain): sedimentation, depositional environments and paleogeographic evolution. *Sed. Geol.*, **160**, 213–242.

Frape, S.K., **Fritz, P.** and **McNutt, R.H.** (1984) Water-rock interaction and chemistry of groundwaters from the Canadian Shield. *Geochim. Cosmochim. Acta*, **48**, 1617–1627.

Frimmel, H.E. (2010) On the reliability of stable carbon isotopes for Neoproterozoic chemostratigraphic correlation. *Precambr. Res.*, **182**, 239–253.

Gerdes, A. and **Zeh, A.** (2009) Zircon formation versus zircon alteration—new insights from combined U-Pb and Lu-Hf in situ LA-ICP-MS analyzes, and consequences for the interpretation of Archean zircon from the Central Zone of the Limpopo Belt. *Chem. Geol.*, **261**, 230–243.

Geske, A., **Zorlu, J.**, **Richter, D.K.**, **Buhl, D.**, **Niedermayr, A.** and **Immenhauser, A.** (2012) Impact of diagenesis and low grade metamorphosis on isotope (δ^{26}Mg, δ^{13}C, δ^{18}O and ^{87}Sr/^{86}Sr) and elemental (Ca, Mg, Mn, Fe and Sr) signatures of Triassic sabkha dolomites. *Chem. Geol.*, **332–333**, 45–64.

Geske, A., **Goldstein, R.H.**, **Mavromatis, V.**, **Richter, D.K.**, **Buhl, D.**, **Kluge, T.**, **John, C.M.** and **Immenhauser, A.** (2015a) The magnesium isotope (δ^{26}Mg) signature of dolomites. *Geochim. Cosmochim. Acta*, **149**, 131–151.

Geske, A., **Lokier, S.**, **Dietzel, M.**, **Richter, D.K.**, **Buhl, D.** and **Immenhauser, A.** (2015b) Magnesium isotope composition of sabkha porewater and related (Sub-)Recent stoichiometric dolomites, Abu Dhabi (UAE). *Chem. Geol.*, **393–394**, 112–124.

Goldstein, R.H. and **Reynolds, T.J.** (1994) *Systematics of Fluid Inclusions in Diagenetic Minerals*. Short Course 31, Society of Economic Paleontologists and Mineralogists, Tulsa, 199 pp.

Grossman, E.L. (2012) Applying oxygen isotope paleothermometry in deep time. *Paleontol. Soc. Pap.*, **18**, 39–67.

Grotzinger, J.P., **Fike, D.A.** and **Fischer, W.W.** (2011) Enigmatic origin of the largest-known carbon isotope excursion in Earth's history. *Nat. Geosci.*, **4**, 285–292.

Halverson, G.P., **Hoffman, P.F.**, **Schrag, D.P.**, **Maloof, A.C.** and **Rice, A.H.N.** (2005) Toward a Neoproterozoic composite carbon-isotope record. *Geol. Soc. Am. Bull.*, **117**, 1181–1207.

Hardie, L.A. (1996) Secular variation in seawater chemistry: An explanation for the coupled secular variation in the mineralogies of marine limestones and potash evaporites over the past 600 m.y. *Geology*, **24**, 279–283.

Hendry, J.P., **Gregg, J.M.**, **Shelton, K.L.**, **Somerville, I.D.** and **Crowley, S.F.** (2015) Origin, characteristics and distribution of fault-related and fracture-related dolomitization: Insights from Mississippian carbonates, Isle of Man. *Sedimentology*, **62**, 717–752.

Hohl, S.V., **Galer, S.J.G.**, **Gamper, A.** and **Becker, H.** (2017) Cadmium isotope variations in Neoproterozoic carbonates – a tracer of biologic production? *Geochem. Perspect. Lett.*, **3**, 32–44.

Hood, A.S., **Wallace, M.W.** and **Drysdale, R.N.** (2011) Neoproterozoic aragonite-dolomite seas? Widespread marine dolomite precipitation in Cryogenian reef complexes. *Geology*, **39**, 871–874.

Hood, A.S., **Planavsky, N.J.**, **Wallace, M.W.** and **Wang, X.** (2018) The effects of diagenesis on geochemical paleoredox proxies in sedimentary carbonates. *Geochim. Cosmochim. Acta*, **232**, 265–287.

Hu, W., **Wang, X.**, **Zhu, D.**, **You, D.** and **Wu, H.** (2018) An overview of types and characterization of hot fluids associated with reservoir formation in petroliferous basins. *Energy Explor. Exploit.*, 1–17.

Ingebritsen, S.E. and **Sanford, W.E.** (1998) *Groundwater in Geologic Processes*. Cambridge University Press, Cambridge, UK.

Jacquemyn, C., **El Desouky, H.**, **Hunt, D.**, **Casini, G.** and **Swennen, R.** (2014) Dolomitization of the latemar platform: Fluid flow and dolomite evolution. *Mar. Pet. Geol.*, **55**, 43–67.

James, N.P. and **Choquette, P.W.** (1990) Diagenesis 9. Limestones – the meteoric diagenetic environment. In: *Diagenesis* (Eds L.A. McIlreath and D.W. Morrow), Geoscience Canada Reprint Series, **4**, 161–194.

Jenkins, R.J.F., **McKirdy, D.M.**, **Foster, C.B.**, **O'Leary, T.** and **Pell, S.D.** (1992) The record and stratigraphie implications of organic-walled microfossils from the Ediacaran (terminal Proterozoic) of South Australia. *Geol. Mag.*, **129**, 401–410.

Johnson, C. (1993) Contrasted thermal histories of different nappe complexes in SE Spain: evidence for complex crustal extension. In: *Late Orogenic Extension in Mountain Belts* (Eds M. Stranne and J. Malavielle). Dot. BGRM Fr. No., **299**, 103.

Johnston, D.T., **Poulton, S.W.**, **Dehler, C.**, **Porter, S.**, **Husson, J.**, **Canfield, D.E.** and **Knoll, A.H.** (2010) An emerging picture of Neoproterozoic ocean chemistry: Insights from the Chuar Group, Grand Canyon, USA. *Earth Planet. Sci. Lett.*, **290**, 64–73.

Jonas, L., **Müller, T.**, **Dohmen, R.**, **Immenhauser, A.** and **Pulitz, B.** (2017) Hydrothermal replacement of biogenic and abiogenic aragonite by Mg-carbonates - Relation between textural control on effective element fluxes and resulting carbonate phase. *Geochim. Cosmochim. Acta*, **196**, 289–306.

Kamber, B.S. and **Webb, G.E.** (2001) The geochemistry of late Archaean microbial carbonate: implications for ocean chemistry and continental erosion history. *Geochim. Cosmochim. Acta*, **65**, 2509–2525.

Kampschuur, W. and **Rondeel, H.E.** (1975) The origin of the Betic orogen, southern Spain. *Tectonophysics*, **27**, 39–56.

Kasemann, S.A., **Hawkesworth, C.J.**, **Prave, A.R.**, **Fallick, A.E.** and **Pearson, P.N.** (2005) Boron and calcium isotope composition in Neoproterozoic carbonate rocks from Namibia: evidence for extreme environmental change. *Earth Planet. Sci. Lett.*, **231**, 73–86.

Kasemann, S.A., **Pogge von Strandmann, P.A.E.**, **Prave, A.R.**, **Fallick, A.E.**, **Elliott, T.** and **Hoffmann, K.-H.** (2014) Continental weathering following a Cryogenian glaciation: Evidence from calcium and magnesium isotopes. *Earth Planet. Sci. Lett.*, **396**, 66–77.

Kaufman, A.J. and **Knoll, A.H.** (1995) Neoproterozoic variations in the carbon-isotopic composition of seawater: stratigraphic and biogeochemical implications. *Precambrian Res.*, **73**, 27–50.

Keller, J.V.A., **Hall, S.H.**, **Dart, C.J.** and **McClay, K.R.** (1995) The geometry and evolution of a transpressional strike-slip system: the Carboneras fault, SE Spain. *J. Geol. Soc.*, **152**, 339–351.

Knauth, L.P. and **Kennedy, M.J.** (2009) The late Precambrian greening of the Earth. *Nature*, **460**, 728–732.

Koehn, D., **Ebner, M.**, **Renard, F.**, **Toussaint, R.** and **Passchier, C.W.** (2012) Modelling of stylolite geometries and stress scaling. *Earth Planet. Sci. Lett.*, **341–344**, 104–113.

Korte, C., **Kozur, H.W.**, **Bruckschen, P.** and **Veizer, J.** (2003) Strontium isotope evolution of Late Permian and Triassic seawater. *Geochim. Cosmochim. Acta*, **67**, 47–62.

Lambert, I.B., **Walter, M.R.**, **Wenlong, Z.**, **Songnian, L.** and **Guogan, M.** (1987) Palaeoenvironment and carbon isotope stratigraphy of Upper Proterozoic carbonates of the Yangtze Platform. *Nature*, **325**, 140–142.

Land, L.S. (1980) The isotopic and trace element geochemistry of dolomite: the state of the art. *SEPM Spec. Publ.*, **28**, 87–110.

Lohmann, K.C. (1987) Geochemical patterns of meteoric diagenetic systems and their application to the study of paleokarst. In: *Paleokarst*(Eds. N.P. James and P.W. Choquette), pp. 58–80. Springer-Verlag, Berlin.

Lonergan, L. (1993) Timing and kinematics of deformation in the Malaguide Complex, internal zone of the Betic Cordillera, southeast Spain. *Tectonics*, **12**, 460–476.

Lonergan, L. and **Platt, J.P.** (1995) The Malaguide-Alpujarride boundary: a major extensional contact in the Internal Zone of the eastern Betic Cordillera, SE Spain. *J. Struct. Geol.*, **17**, 1655–1671.

López-Horgue, M.A., **Iriarte, E.**, **Schröder, S.**, **Fernández-Mendiola, P.A.**, **Caline, B.**, **Corneyllie, H.**, **Frémont, J.**, **Sudrie, M.** and **Zerti, S.** (2010) Structurally controlled hydrothermal dolomites in Albian carbonates of the Asón valley, Basque Cantabrian Basin, Northern Spain. *Mar. Pet. Geol.*, **27**, 1069–1092.

Loyd, S.J., **Corsetti, F.A.**, **Eagle, R.A.**, **Hagadorn, J.W.**, **Shen, Y.**, **Zhang, X.**, **Bonifacie, M.** and **Tripati, A.K.** (2015) Evolution of Neoproterozoic Wonoka-Shuram Anomaly-aged carbonates: Evidence from clumped isotope paleothermometry. *Precambr. Res.*, **264**, 179–191.

Ludwig, K. (2007) Isoplot 3.62. *Berkeley Geochronol. Center Spec. Publ.*, **4**, 70.

Magaritz, M., **Holser, W.T.** and **Kirschvink, J.L.** (1986) Carbon isotope events across the Precambrian/Cambrian boundary on the Siberian platform. *Nature*, **320**, 258–259.

Maillard, A. and **Mauffret, A.** (1999) Crustal structure and riftogenesis of the Valencia Trough (north-western Mediterranean Sea). *Basin Res.*, **11**, 357–379.

Martín, J.M. (1978) Evolución, diagenética de un sector de los materiales carbonatados de la Unidad Viboras (Mantos Alpujárrides, NW Sierra Nevada). *Bol. Geol. Min. Madrid*, **88**, 303–319.

Martín, J.M. and **Braga, J.C.** (1987) Alpujárride carbonate deposits (Southern Spain) - marine sedimentation in a Triassic Atlantic. *Palaeogeogr. Palaeoclimatol. Palaeoecol.*, **59**, 243–260.

Martín, J.M., **Braga, J.C.** and **Betzler, C.** (2003) Late Neogene–Recent uplift of the Cabo de Gata volcanic province, Almería, SE Spain. *Geomorphology*, **50**, 27–42.

Martín-Martín, J.D., **Travé, A.**, **Gomez-Rivas, E.**, **Salas, R.**, **Sizun, J.-P.**, **Vergés, J.**, **Corbella, M.**, **Stafford, S.L.** and **Alfonso, P.** (2015) Fault-controlled and stratabound dolostones in the Late Aptian–earliest Albian Benassal Formation (Maestrat Basin, E Spain): Petrology and geochemistry constrains. *Mar. Pet. Geol.*, **65**, 83–102.

Mattei, M., **Riggs, N.R.**, **Giordano, G.**, **Guarnieri, L.**, **Cifelli, F.**, **Soriano, C.C.**, **Jicha, B.**, **Jasmin, A.**, **Marchionni, S.**, **Franciosi, L.**, **Tommasini, S.**, **Porreca, M.** and **Conticelli, S.** (2014) Geochronology, geochemistry and geodynamics of the Cabo de Gata volcanic zone, Southeastern Spain. *Ital. J. Geosci.*, **133**, 341–361.

Mavromatis, V., **Purgstaller, B.**, **Dietzel, M.**, **Buhl, D.**, **Immenhauser, A.** and **Schott, J.** (2017) Impact of amorphous precursor phases on magnesium isotope signatures of Mg-calcite. *Earth Planet. Sci. Lett.*, **464**, 227–236.

Mazumdar, A. and **Strauss, H.** (2006) Sulfur and strontium isotopic compositions of carbonate and evaporite rocks from the late Neoproterozoic–early Cambrian Bilara Group (Nagaur-Ganganagar Basin, India): constraints on intrabasinal correlation and global sulfur cycle. *Precambr. Res.*, **149**, 217–230.

McArthur, J.M., **Howarth, R.J.** and **Shields, G.A.** (2012) Strontium isotope stratigraphy. In: *The Geologic Time Scale*, 1st edn (Eds F.M. Gradstein, J.G. Ogg, M.D. Schmitz and G.M. Ogg), pp. 127–144. Elsevier BV, Oxford.

McKenzie, J.A. (1981) Holocene dolomitization of calcium carbonate sediments from the coastal Sabkhas of AbuDhabi, U.A.E.: a Stable Isotope Study. *J. Geol.*, **89**, 185–198.

Melezhik, V.A., **Pokrovsky, B.G.**, **Fallick, A.E.**, **Kuznetsov, A.B.** and **Bujakaite, M.I.** (2009) Constraints on Sr-87/Sr-86 of Late Ediacaran seawater: insight from Siberian high-Sr limestones. *J. Geol. Soc.*, **166**, 183–191.

Meyer, M., **Brockamp, O.**, **Clauer, N.**, **Renk, A.** and **Zuther, M.** (2000) Further evidence for a Jurassic mineralizing event in central Europe: K-Ar dating of hydrothermal alteration and fluid inclusion systematics in wall rocks of the Käfersteige fluorite vein deposit in the northern Black Forest, Germany. *Miner. Deposita*, **35**, 754–761.

Molli, G., **Vitale Brovarone, A.**, **Beyssac, O.** and **Cinquini, I.** (2018) RSCM thermometry in the Alpi Apuane (NW Tuscany, Italy): New constraints for the metamorphic and tectonic history of the inner northern Apennines. *J. Struct. Geol.*, **113**, 200–216.

Monie, P., **Galindo-Zaldivar, J.**, **Lodeiro, F.G.**, **Goffe, B.** and **Jabaloy, A.** (1991) $^{40}Ar/^{39}Ar$ geochronology of Alpine tectonism in the Betic Cordilleras (southern Spain). *J. Geol. Soc.*, **148**, 289–297.

Moreno, X., **Masana, E.**, **Pallàs, R.**, **Gràcia, E.**, **Rodés, Á.** and **Bordonau, J.** (2015) Quaternary tectonic activity of the Carboneras Fault in the La Serrata range (SE Iberia): Geomorphological and chronological constraints. *Tectonophysics*, **663**, 78–94.

Morrow, D.W. (2014) Zebra and boxwork fabrics in hydrothermal dolomites of northern Canada: Indicators for

dilational fracturing, dissolution or in situ replacement? *Sedimentology*, **61**, 915–951.

Munoz, M., **Baron, S.**, **Boucher, A.**, **Béziat, D.** and **Salvi, S.** (2016) Mesozoic vein-type Pb–Zn mineralization in the Pyrenees: Lead isotopic and fluid inclusion evidence from the Les Argentières and Lacore deposits. *C.R. Geosci.*, **348**, 322–332.

Nagarajan, R., **Armstrong-Altrin, J.**, **Sial, A.**, **Nagendra, R.** and **Ellam, R.** (2013) Carbon, oxygen, and strontium isotope geochemistry of the Proterozoic carbonate rocks, Bhima basin, south India: Implication for diagenesis. *Carpathian J. Earth Environ. Sci.*, **8**, 25–38.

Neuser, R.D., **Bruhn, F.**, **Götze, J.**, **Habermann, D.** and **Richter, D.K.** (1996) Kathodoluminseszenz: Methodik und Anwendung [Cathodoluminescence: method and application]. *Zbl. Geol. Paläont. Teil*, **1**, 287–206.

Nordeng, S.H. and **Sibley, D.F.** (1994) Dolomite stoichiometry and Ostwald's Step Rule. *Geochim. Cosmochim. Acta*, **58**, 191–196.

Patterson, R.J. and **Kinsman, D.J.J.** (1982) Formation of diagenetic dolomite in Coastal Sabkha along Arabian (Persian) Gulf. *AAPG Bull.*, **66**, 28–43.

Pederson, C., **Mavromatis, V.**, **Dietzel, M.**, **Rollion-Bard, C.**, **Nehrke, G.**, **Jöns, N.**, **Jochum, K.P.** and **Immenhauser, A.** (2019) Diagenesis of mollusc aragonite and the role of fluid reservoirs. *Earth Planet. Sci. Lett.*, **514**, 130–142.

Perry, E.A.J. and **Turekian, K.K.** (1974) The effects of diagenesis on the redistribution of strontium isotopes in shales. *Geochim. Cosmochim. Acta*, **38**, 929–935.

Petrash, D.A., **Bialik, O.M.**, **Bontognali, T.R.R.**, **Vasconcelos, C.**, **Roberts, J.A.**, **McKenzie, J.A.** and **Konhauser, K.O.** (2017) Microbially catalyzed dolomite formation: from near-surface to burial. *Earth Sci. Rev.*, **171**, 558–582.

Pfaff, K., **Romer, R.L.** and **Markl, G.** (2009) U-Pb ages of ferberite, chalcedony, agate, 'U-mica' and pitchblende: constraints on the mineralization history of the Schwarzwald ore district. *Eur. J. Mineral.*, **21**, 817–836.

Pingitore, N.E., Jr (1982) The role of diffusion during carbonate diagenesis. *J. Sediment. Petrol.*, **52**, 27–39.

Platt, J.P. and **Vissers, R.L.M.** (1989) Extensional collapse of thickened continental lithosphere: A working hypothesis for the Alboran Sea and Gibraltar arc. *Geology*, **17**, 540–543.

Platt, J.P., **Kelley, S.P.**, **Carter, A.** and **Orozco, M.** (2005) Timing of tectonic events in the Alpujárride Complex, Betic Cordillera, southern Spain. *J. Geol. Soc.*, **162**, 451–462.

Qing, H., **Bosence, D.W.J.** and **Rose, E.P.F.** (2001) Dolomitization by penesaline sea water in Early Jurassic peritidal platform carbonates, Gibraltar, western Mediterranean. *Sedimentology*, **48**, 153–163.

Radke, B.M. and **Mathis, R.L.** (1980) On the formation and occurrence of saddle dolomite. *J. Sediment. Res.*, **50**, 1149–1168.

Renard, F., **Schmittbuhl, J.**, **Gratier, J.P.**, **Meakin, P.** and **Merino, E.** (2004) Three- dimensional roughness of stylolites in limestones. *J. Geophys. Res.*, **109**, 1–12.

Richter, D.K., **Heinrich, F.**, **Geske, A.**, **Neuser, R.D.**, **Gies, H.** and **Immenhauser, A.** (2014) First description of Phanerozoic radiaxial fibrous dolomite. *Sed. Geol.*, **304**, 1–10.

Roep, T.B. (1972) Stratigraphy of the Permo-Triassic Saladilla formation and its tectonic setting in the Betic of Malaga (Velez Rubio region, SE Spain). *K. Ned. Akad. Wet. Ser. B*, **75**, 223–247.

Rott, C.M. and **Qing, H.** (2013) Early dolomitization and recrystallization in shallow marine carbonates, Mississippian Alida Beds, Williston Basin (Canada): Evidence from petrography and isotope geochemistry. *J. Sediment. Res.*, **83**, 928–941.

Rutter, E.H., **Faulkner, D.R.** and **Burgess, R.** (2012) Structure and geological history of the Carboneras Fault Zone, SE Spain: Part of a stretching transform fault system. *J. Struct. Geol.*, **45**, 68–86.

Rutter, E.H., **Burgess, R.** and **Faulkner, D.R.** (2014) Constraints on the movement history of the Carboneras Fault Zone (SE Spain) from stratigraphy and ^{40}Ar–^{39}Ar dating of Neogene volcanic rocks. *Geol. Soc. London Spec. Publ.*, **394**, 79–99.

Saltzman, M.R. and **Thomas, E.** (2012) Carbon isotope stratigraphy. In: *The Geologic Time Scale*, 1st edn (Eds F.M. Gradstein, J.G. Ogg, M.D. Schmitz and G.M. Ogg), pp. 207–232. Elsevier BV, Oxford.

Sandberg, P.A. (1983) An oscillating trend in Phanerozoic non-skeletal carbonate mineralogy. *Nature*, **305**, 19–22.

Sanz de Galdeano, C. and **López Garrido, A.C.** (2014) Structure of the Sierra de Lujar (Alpujarride Complex, Betic Cordillera). *Estud. Geol.*, **70**, e005.

Sanz de Galdeano, C., **Andreo, B.**, **García-Tortosa, F.J.** and **López-Garrido, A.C.** (2001) The Triassic palaeogeographic transition between the Alpujarride and Malaguide complexes. Betic-Rif Internal Zone (S Spain, N Morocco). *Palaeogeogr. Palaeoclimatol. Palaeoecol.*, **167**, 157–173.

Shen, Y., **Zhao, R.**, **Chu, X.** and **Lei, J.** (1998) The carbon and sulfur isotope signatures in the Precambrian-Cambrian Transition series of the Yangtze Platform. *Precambr. Res.*, **89**, 77–86.

Shepherd, T.J., **Rankin, A.H.** and **Alderton, D.H.M.** (1985) *A Practical Guide to Fluid Inclusion Studies*. Glasgow and London (Blackie), xi +, 239 pp.

Shuster, A.M., **Wallace, M.W.**, **van Smeerdijk Hood, A.** and **Jiang, G.** (2018) The Tonian Beck Spring Dolomite: Marine dolomitization in a shallow, anoxic sea. *Sed. Geol.*, **368**, 83–104.

Sibley, D.F. and **Gregg, J.M.** (1987) Classification of dolomite rock texture. *J. Sediment. Petrol.*, **57**, 967–975.

Sola, F., **Puga-Bernabéu, Á.**, **Aguirre, J.** and **Braga, J.C.** (2018) Origin, evolution and sedimentary processes associated with a late Miocene submarine landslide, southeast Spain. *Sed. Geol.*, **364**, 351–366.

Steele-MacInnis, M., **Bodnar, R.J.** and **Naden, J.** (2011) Numerical model to determine the composition of H_2O–NaCl–$CaCl_2$ fluid inclusions based on microthermometric and microanalytical data. *Geochim. Cosmochim. Acta*, **75**, 21–40.

Subias, I., **Fanlo, I.** and **Billström, K.** (2015) Ore-forming timing of polymetallic-fluorite low temperature veins from Central Pyrenees: A Pb, Nd and Sr isotope perspective. *Ore Geol. Rev.*, **70**, 241–251.

Swart, P.K. (2015) The geochemistry of carbonate diagenesis: The past, present and future. *Sedimentology*, **62**, 1233–1304.

Tera, F. and **Wasserburg, G.J.** (1972) U-Th-Pb systematics in three Apollo 14 basalts and the problem of initial Pb in lunar rocks. *Earth Planet. Sci. Lett.*, **14**, 281–304.

Tipper, E., **Galy, A.**, **Gaillardet, J.**, **Bickle, M.**, **Elderfield, H.** and **Carder, E.** (2006) The magnesium isotope budget of the modern ocean: Constraints from riverine magnesium isotope ratios. *Earth Planet. Sci. Lett.*, **250**, 241–253.

Torres-Roldán, R.L. (1979) The tectonic subdivision of the Betic Zone (Betic Cordilleras, southern Spain); its significance and one possible geotectonic scenario for the westernmost Alpine Belt. *Am. J. Sci.*, **279**, 19–51.

Tritlla, J. and **Sole, J.** (1999) A newly dated Cretaceous hydrothermal event in the Iberian Ranges (Eastern Spain) and its significance within the Mesozoic thermal history within the Iberian Peninsula. *Ore Geol. Rev.*, **15**, 243–259.

Tucker, M.E. (1982) Precambrian dolomites: petrographic and isotopic evidence that they differ from Phanerozoic dolomites. *Geology*, **10**, 7–12.

Tucker, M.E. (1983) Diagenesis, geochemistry, and origin of a Precambrian dolomite: the Beck Spring Dolomite of eastern California. *J. Sediment. Res.*, **53**, 1097–1119.

Turpin, M., **Gressier, V.**, **Bahamonde, J.R.** and **Immenhauser, A.** (2014) Component-specific petrographic and geochemical characterization of fine-grained carbonates along Carboniferous and Jurassic platform-to-basin transects. *Sed. Geol.*, **300**, 62–85.

Van de Poel, H.M. (1992) Foraminiferal biostratigraphy and palaeo-environments of the Miocene-Pliocene Carboneras-Nijar Basin (SE Spain). *Scripta Geol.*, **102**, 1–32.

Vandeginste, V., **Swennen, R.**, **Gleeson, S.A.**, **Ellam, R.M.**, **Osadetz, K.** and **Roure, F.** (2005) Zebra dolomitization as a result of focused fluid flow in the Rocky Mountains Fold and Thrust Belt, Canada. *Sedimentology*, **52**, 1067–1095.

Veizer, J. and **Prokoph, A.** (2015) Temperatures and oxygen isotopic composition of Phanerozoic oceans. *Earth Sci. Rev.*, **146**, 92–104.

Vissers, L.M. (2012) Extension in a convergent tectonic setting: a lithospheric view on the Alboran system of SW Europe. *Geol. Belgica*, **15**, 53–72.

Völk, H.R. and **Rondeel, H.E.** (1964) Zur Gliederung des Jungtertiärs im Becken von Vera, Südostspanien. *Geol. Mijnbouw*, **43**, 310–315.

Wacey, D., **Wright, D.T.** and **Boyce, A.J.** (2007) A stable isotope study of microbial dolomite formation in the Coorong Region, South Australia. *Chem. Geol.*, **244**, 155–174.

Wallace, M.W. and **Hood, A.S.** (2018) Zebra textures in carbonate rocks: Fractures produced by the force of crystallization during mineral replacement. *Sed. Geol.*, **368**, 58–67.

Walter, B.F., **Immenhauser, A.**, **Geske, A.** and **Markl, G.** (2015) Exploration of hydrothermal carbonate magnesium isotope signatures as tracers for continental fluid aquifers, Schwarzwald mining district, SW Germany. *Chem. Geol.*, **400**, 87–105.

Walter, B.F., **Steele-MacInnis, M.** and **Markl, G.** (2017) Sulfate brines in fluid inclusions of hydrothermal veins: compositional determinations in the system H_2O-Na-Ca-Cl-SO_4. *Geochim. Cosmochim. Acta*, **209**, 184–203.

Walter, B.F., **Gerdes, A.**, **Kleinhanns, I.C.**, **Dunkl, I.**, **von Eynatten, H.**, **Kreissl, S.** and **Markl, G.** (2018) The connection between hydrothermal fluids, mineralization, tectonics and magmatism in a continental rift setting: fluorite Sm-Nd and hematite and carbonates U-Pb geochronology from the Rhinegraben in SW Germany. *Geochim. Cosmochim. Acta*, **240**, 11–42.

Watson, E.B. and **Müller, T.** (2009) Non-equilibrium isotopic and elemental fractionation during diffusion-controlled crystal growth under static and dynamic conditions. *Chem. Geol.*, **267**, 111–124.

Weijermars, R. (1991) Geology and tectonics of the Betic Zone, SE Spain. *Earth Sci. Rev.*, **31**, 153–236.

Wetzel, A., **Allenbach, R.** and **Allia, V.** (2003) Reactivated basement structures affecting the sedimentary facies in a tectonically "quiescent" epicontinental basin: an example from NW Switzerland. *Sed. Geol.*, **157**, 153–172.

Wilson, E.N., **Hardie, L.A.** and **Phillips, O.M.** (1990) Dolomitization front geometry, fluid flow patterns, and the origin of massive dolomite: The Triassic Latemar buildup, Northern Italy. *Am. J. Sci.*, **290**, 741–796.

Wood, R.A., **Zhuravlev, A.Y.**, **Sukhov, S.S.**, **Zhu, M.** and **Zhao, F.** (2017) Demise of Ediacaran dolomitic seas marks widespread biomineralization on the Siberian Platform. *Geology*, **45**, 27–30.

Zhou, C., **Guan, C.**, **Cui, H.**, **Ouyang, Q.** and **Wang, W.** (2016) Methane-derived authigenic carbonate from the lower Doushantuo Formation of South China: Implications for seawater sulfate concentration and global carbon cycle in the early Ediacaran ocean. *Palaeogeogr. Palaeoclimatol. Palaeoecol.*, **461**, 145–155.

Zohdi, A., **Moallemi, S.A.**, **Moussavi-Harami, R.**, **Mahboubi, A.**, **Richter, D.K.**, **Geske, A.**, **Nickandish, A.A.** and **Immenhauser, A.** (2014) Shallow burial dolomitization of an Eocene carbonate platform, southeast Zagros Basin, Iran. *GeoArabia*, **19**, 17–54.

Manuscript received 25 February 2019; revision accepted 25 August 2019

Supporting Information

Additional information may be found in the online version of this article:

Appendix A1. Supporting information on methodology and circumstantial data on major and trace elements, geochemical and petrographical results.